Effects of structural distortions on the electronic structure of *T*-type transition metal dichalcogenides

Daniel T. Larson,[1] Wei Chen,[1,2] Steven B. Torrisi,[1] Jennifer Coulter,[3] Shiang Fang,[1,4,*] and Efthimios Kaxiras[1,3,†]

[1]*Department of Physics, Harvard University, Cambridge, Massachusetts 02138, USA*

[2]*Center for Functional Nanomaterials, Brookhaven National Laboratory, Upton, New York 11973, USA*

[3]*John A. Paulson School of Engineering and Applied Sciences, Harvard University, Cambridge, Massachusetts 02138, USA*

[4]*Department of Physics and Astronomy, Center for Materials Theory, Rutgers University, Piscataway, New Jersey 08854, USA*

(Received 25 March 2020; revised 3 July 2020; accepted 7 July 2020; published 20 July 2020)

Single-layer transition metal dichalcogenides (TMDCs) can adopt two distinct structures corresponding to different coordination of the metal atoms. TMDCs adopting the *T*-type structure exhibit a rich and diverse set of phenomena, including charge density waves (CDWs) in a $\sqrt{13} \times \sqrt{13}$ supercell pattern in TaS_2 and $TaSe_2$, and a possible excitonic insulating phase in $TiSe_2$. These properties make the *T*-TMDCs desirable components of layered heterostructure devices. In order to predict the emergent properties of combinations of different layered materials, one needs simple and accurate models for the constituent layers which can take into account potential effects of lattice mismatch, relaxation, strain, and structural distortion. Previous studies have developed *ab initio* tight-binding Hamiltonians for *H*-type TMDCs [S. Fang *et al.*, Phys. Rev. B **98**, 075106 (2018)]. Here we extend this work to include *T*-type TMDCs. We demonstrate the capabilities and limitations of our model using three example systems: a one-dimensional sinusoidal ripple, which represents a longitudinal acoustic phonon; the 2×2 CDW in $TiSe_2$; and the $\sqrt{13} \times \sqrt{13}$ CDW in TaS_2. Using the technique of band unfolding we compare the electronic structure of the distorted crystals to the pristine band structure and find our tight-binding model reproduces many features revealed by direct density functional theory calculations, provided the magnitude of the distortions remains in the linear regime. This model of the strain response of single layers is a necessary ingredient for the construction of models of van der Waals heterostructures with multiple layers, because the deformation and strain from mechanical relaxations in a twisted bilayer have important effects on the electronic structure.

DOI: 10.1103/PhysRevB.102.045128

I. INTRODUCTION

There has been significant progress in the production of van der Waals heterostructures, devices formed by combinations of various two-dimensional layered materials [1]. These layers offer a promising platform for applications in optoelectronics [2], spintronics [3], valleytronics [4], straintronics [5,6], twistronics [7], nanomechanical resonators [8], and plasmonics [9]. Individual layers can be insulators, semimetals, or metals, and can express many different quantum orders, including charge density waves (CDWs) [10], superconductivity (SC) [11], magnetism [12–14], topological phases [15,16], and Mott-insulator physics [17–20].

Transition metal dichalcogenides (TMDCs) are an interesting class of materials formed by a layer of transition metal atoms (M) sandwiched between layers of chalcogens (X) with the chemical formula MX_2, as shown in Fig. 1. TMDCs built from group-VI transition metals, such as Mo and W, generally take on the *H* structure in which the transition metal exhibits trigonal prismatic coordination by the chalcogens (point group D_{3h}), as shown in Figs. 1(c) and 1(d). These materials, which are usually semiconductors, have become the subject of investigation for the past several years. TMDCs can also crystallize in the *T* structure, in which the metal atom is octahedrally coordinated by the chalcogens (point group D_{3d}), as shown in Figs. 1(a) and 1(b). For TMDCs containing group-IV or -V transition metals, the *T* structure is typically metallic and either more stable or very close in energy to the *H* phase. These *T*-type TMDCs, or *T*-TMDCs, are gaining attention because of their rich quantum phases. For example, with decreasing temperature, $1T$-TaS_2 transitions from a high-temperature normal metallic phase to an incommensurate CDW, near-commensurate CDW, and finally a commensurate CDW with "Star of David" clusters of Ta atoms with a $\sqrt{13} \times \sqrt{13}$ periodicity [21] that gives rise to an insulating phase that might be a correlated Mott phase, at least for single layers [22], but might also reflect effects of the stacking order between layers [23–25]. Under pressure, the insulating phase melts and superconductivity develops around 2.5 GPa with T_c saturating at 5 K under high pressure [26]. In addition, there is a suggestion that TaS_2 should be considered a quantum spin liquid [19].

In these *T*-type TMDCs, the existence of various electronic phases provides a platform to study their mutual competition and quantum criticality. Empirical tight-binding models

*shiangfang913@gmail.com
†kaxiras@physics.harvard.edu

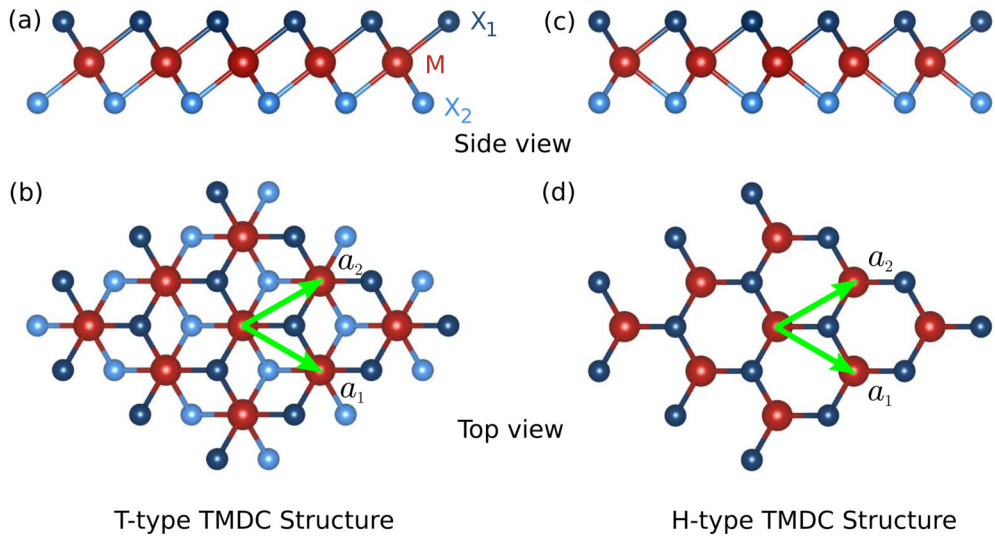

FIG. 1. T-type TMDC crystal structure seen from the (a) side and (b) top. For comparison we show the H-type TMDC crystal from the (c) side and (d) top, respectively. $\boldsymbol{a}_1$ and $\boldsymbol{a}_2$ are the primitive lattice vectors of the two-dimensional (2D) crystal (green arrows).

have been constructed for the Ti-based T-TMDCs [27] and for TaS_2 [28]. However, theoretical models for these T-type TMDCs are scarce compared to their H-type counterparts. In this work we provide comprehensive *ab initio* tight-binding Hamiltonians (TBHs) for nine different T-type TMDCs, considering the d orbitals from transition metal atoms and the p orbitals from the chalcogens. These Hamiltonians are extracted from the Wannier transformation of density functional theory (DFT) calculations without parameter fitting. In-plane strain is also included in the Hamiltonian modeling, capturing the coupling between electrons and long-wavelength acoustic phonon modes. This provides a simple "parent" electronic band structure in which additional perturbations from CDW order or other deformations can be introduced, as long as the atomic displacements from the parent structure are not too large. The application of symmetry group analysis simplifies the modeling and elucidates the nature of the various coupling terms.

Tight-binding models of strained TMDCs can also be empirically built using the Slater-Koster parametrization and reasonable assumptions about the scaling of the hopping parameters with distance, as has been done for H-type TMDCs such as MoS_2 [29]. By extracting hopping parameters from the overlap of Wannier functions, the present method is naturally free of any assumptions about the shape or scaling of the tight-binding orbitals. The price for the increased accuracy is that it might obscure approximate relationships between the parameters. That makes the present approach better suited to the accurate numerical simulation of large-scale structures including nonuniform relaxation, as opposed to simpler, qualitative models geared towards intuitive understanding.

This paper is organized as follows: In Sec. II we survey some of the notable properties of the T-TMDC materials we have modeled. In Sec. III we provide details of the modeling procedure and give the explicit symmetry-constrained form of the tight-binding Hamiltonian that includes strain perturbations. Validation and analysis is provided in Sec. IV, followed by applications to three model systems in Sec. V, and finally our conclusions in Sec. VI. In the Appendix we tabulate the material-dependent numerical parameters extracted from DFT calculations for these tight-binding Hamiltonians.

II. T-TYPE TMDC MATERIAL PROPERTIES

Strain-dependent tight-binding models for group-VI TMDCs have been derived in previous work [30]. For these materials, specifically MX_2 (with $M =$ Mo, W and $X =$ S, Se), the H structure is more stable than the T structure, and most are semiconductors. In contrast, here we study group-IV and group-V TMDCs, with $M =$ Ti, Nb, Ta and $X =$ S, Se, Te, where the H and T phases are very close in energy, as shown in Table I. The T phase of the Ti compounds has a lower ground-state energy than the H phase, and for the group-V metals (Nb and Ta) the T phase is within 100 meV

TABLE I. Summary of the single-layer T-type TMDCs considered, showing the calculated energy difference between single layers of the pristine T and H phases, $\Delta E = E_T - E_H$, in units of eV per formula unit (MX_2), and the lattice distortions that have been observed in the various T-phase crystals as multiples of the primitive unit cell, with references where these phases were observed. The last column contains the work function, $\Delta\Phi = E_{\text{vac}} - E_{\text{F}}$ (in eV), discussed later in Sec. III D, for the relaxed, unstrained lattices.

Material	ΔE (eV)	T-structure CDW	$\Delta\Phi$ (eV)
TiS_2	−0.43		5.64
$TiSe_2$	−0.36	2×2 [31]	5.22
$TiTe_2$	−0.31	2×2 [32]	4.70
NbS_2	0.10		5.20
$NbSe_2$	0.09	$\sqrt{13} \times \sqrt{13}$ [17]	4.80
$NbTe_2$	0.00	3×1 [33]	4.51
TaS_2	0.07	$\sqrt{13} \times \sqrt{13}$ [34]	4.95
$TaSe_2$	0.07	$\sqrt{13} \times \sqrt{13}$ [35]	4.57
$TaTe_2$	0.00	3×1, 3×3 [36]	4.32

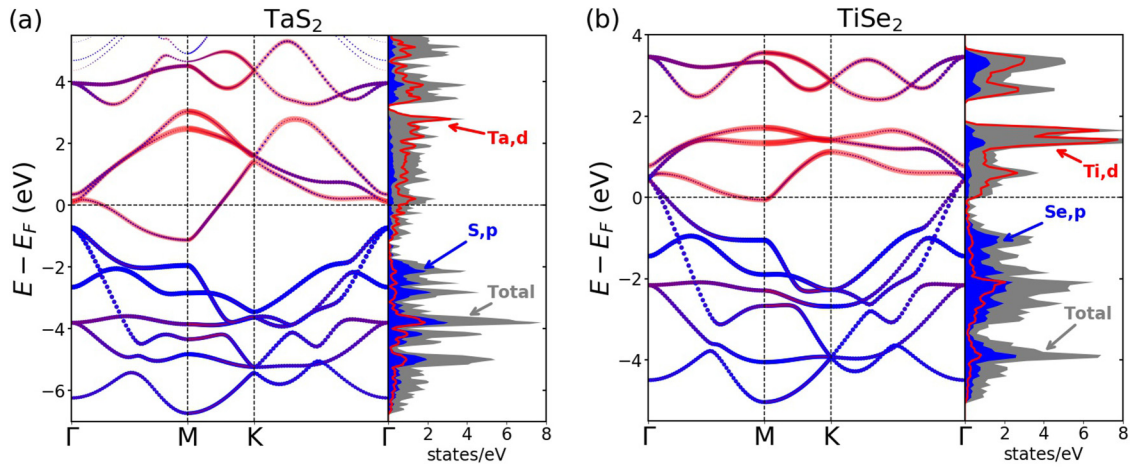

FIG. 2. DFT band structure and density of states (DOS) for two T-type TMDCs, (a) TaS_2 and (b) $TiSe_2$, showing the 11 bands nearest the Fermi level. The valence-band character is dominated by the chalcogen p orbitals, while the transition metal d orbitals dominate the conduction-band character. A notable feature is the large peak in the conduction-band DOS for $TiSe_2$ which is absent for TaS_2.

of the H phase. The values in Table I are the calculated energies of the materials in the undistorted T structure, which have metallic band structures; examples are shown in Fig. 2. The energies shown in Table I represent pristine unit cells in vacuum; in experimental contexts many factors, such as the presence of CDW distortions, substrates, finite temperature, chemical environment and intercalation, strain, and pressure, will affect the stability or metastability of a given phase [37–40]. The T-TMDCs we study are noteworthy for the diversity of CDW patterns which can both stabilize the structure and change the electronic properties. Table I lists the various CDW patterns that have been observed in monolayer or bulk samples. Furthermore, because the H-type to T-type transition can occur via a shift of a chalcogen layer, the kinetic barrier between the phases can be small enough for *in situ* manipulation; for instance, voltage pulses from a scanning tunneling microscope (STM) tip have been shown to reversibly control a transition between H- and T-type structures in $NbSe_2$ [41].

Because of these diverse CDW orders and the interplay with superconductivity, group-IV and group-V TMDCs have been the subject of much recent research. In the following we provide a brief summary of the most interesting features of each of type of material as motivation for the strain-dependent electronic structure modeling described in the next section. More comprehensive reviews and additional references can be found in Refs. [42–44].

$TiSe_2$ is intriguing because it exhibits a 2×2 CDW, a possible excitonic insulating phase [45], and, with doping to suppress the CDW state, superconductivity [46,47]. As a result, the CDW phase has been the subject of study in relation to electronic, excitonic, and vibrational structure effects, and much ongoing investigation focuses on the nature of the CDW transition [48–50]. Single-layer $TiTe_2$ also exhibits a 2×2 CDW, but it is not observed in samples with two or more layers [32]. Previous theoretical work has shown that single-layer TiS_2 is a semimetal with increasing band overlap under compressive strain, but switches to a semiconductor with a gap that grows with tensile strain [51].

NbS_2 and $NbSe_2$ have proven to be challenging to produce in the $1T$ structure. There is a single report of experimental production of the $1T$ polytype of NbS_2 using atmospheric pressure chemical vapor deposition [52]. Recently, Nakata *et al.* [17] have successfully grown single-layer $NbSe_2$ on bilayer graphene and shown that the phase, T vs H, can be controlled by the substrate temperature during growth. It has also been demonstrated that the interaction between an STM tip and the sample can induce a reversible $2H$ to $1T$ phase transition in $NbSe_2$ [41]. On the other hand, bulk $NbTe_2$ takes on the $1T$ structure but with a significant 3×1 CDW distortion [33], and also exhibits superconductivity at temperatures below 1 K [53]. The niobium-based TMDCs are d^1 materials, so the simplest ionic picture would predict metallic behavior with a single half-filled band crossing the Fermi surface. However, angle-resolved photoemission spectroscopy (ARPES) measurements on $NbSe_2$ [17] and $NbTe_2$ [33] do not show any quasiparticle crossings.

The tantalum-based TMDCs are perhaps best known for their rich CDW phases competing with superconductivity. TaS_2 and $TaSe_2$ are formally d^1 materials and are indeed metallic at high temperatures, but as the temperature is lowered they develop incommensurate, nearly commensurate, and finally a commensurate $\sqrt{13} \times \sqrt{13}$ CDW phase. There is not yet strong consensus as to the precise nature of this last insulating phase of TaS_2. Originally understood as being due to Mott physics [22], more recent work has highlighted the importance of the stacking order of the 2D layers and the related orbital ordering [23–25]. In contrast, bulk $TaSe_2$ is metallic even below the CDW transition and only becomes insulating in the monolayer limit [54]. When the CDW phase is suppressed by chemical doping, applying high pressure, or chalcogen substitution, superconductivity can arise at temperatures of a few degrees Kelvin [26,55–57]. On the other hand, $TaTe_2$ exhibits similar behavior to $NbTe_2$ at room temperature, including a 3×1 CDW reconstruction, but at temperatures below ~170 K it displays a competing 3×3 CDW [36] and no superconductivity [33].

III. TIGHT-BINDING HAMILTONIAN FOR THE MONOLAYER WITH STRAIN

A. Numerical methods

DFT calculations were performed using the VASP code [58,59] with the Perdew-Burke-Ernzerhof exchange-correlation functional [60]. Projector augmented wave (PAW) pseudopotentials included 6 valence electrons (s^2p^4) for the chalcogens and 11, 12, and 13 valence electrons for Ta ($5p^6 6s^1\, 5d^4$), Ti ($3s^2\, 3p^6\, 4s^1\, 3d^3$), and Nb ($4s^2\, 4p^6\, 5s^1\, 4d^4$), respectively. A plane-wave energy cutoff of 420 eV was used for all materials, along with van der Waals corrections using the zero-damping DFT-D3 method [61], so that the computational framework can be immediately extended to the study of bilayers in a future publication. We employed a Γ-centered $25 \times 25 \times 1$ k-point grid. All structural relaxations were carried out until the Hellman-Feynman forces on each atom had a magnitude below 0.001 eV/Å. The maximally localized Wannier transformations were performed using the WANNIER90 code [62].

B. General formulation of strained crystal lattices

As viewed from above in Fig. 1(b), the TMDCs T structure consists of three interpenetrating triangular lattices. Seen from the side, the transition metal lattice is sandwiched between chalcogen lattices above and below, in such a way that the metal atom is octahedrally coordinated. To model a monolayer T TMDC we choose the primitive lattice vectors to be $\boldsymbol{a}_1 = \frac{\sqrt{3}}{2}a\hat{x} - \frac{1}{2}a\hat{y}$ and $\boldsymbol{a}_2 = \frac{\sqrt{3}}{2}a\hat{x} + \frac{1}{2}a\hat{y}$. The metal atom is located at the origin and the horizontal position of the upper (lower) chalcogen atom is taken to be $\pm(\boldsymbol{a}_1 + \boldsymbol{a}_2)/3$.

Effects of in-plane strain on the electronic structure can be studied in the same way as they were for H-type TMDCs [30], namely, by displacing the crystal coordinates according to a vector field $\boldsymbol{u} = (u_x(x, y), u_y(x, y))$, where $\boldsymbol{r} = (x, y)$ gives the coordinates in the unstrained crystal and the location in the strained crystal is given by $\boldsymbol{r} + \boldsymbol{u}$. Since no physical change arises from a constant displacement, the strain field is characterized by the symmetrized derivative of $\boldsymbol{u}$ and written as

$$u_{ij} = \tfrac{1}{2}(\partial_i u_j + \partial_j u_i)$$

with $i, j = x, y$. Under the C_{3v} symmetry group of the crystal the strain field can be decomposed into a scalar part, $u_{xx} + u_{yy}$, representing biaxial isotropic strain, and a doublet, $(u_{xx} - u_{yy}, -2u_{xy})$, representing anisotropic strain and shear. The antisymmetrized derivative $\omega_{xy} = \frac{1}{2}(\partial_x u_y - \partial_y u_x)$ is also a scalar under rotations and represents a local rotation of the coordinates by an angle ω_{xy}.

For a constant strain field the lattice vectors are modified as follows:

$$a'_{ix} = a_{ix} + u_{xx}a_{ix} + u_{yx}a_{iy}, \tag{1}$$

$$a'_{iy} = a_{iy} + u_{xy}a_{ix} + u_{yy}a_{iy}, \tag{2}$$

$$a'_{iz} = a_{iz}. \tag{3}$$

By calculating the electronic structure of the crystal subjected to different amounts of uniform strain ($u_{ij} = \text{const}$), we can then approximate the response to a slowly varying strain field by assuming a constant strain over any small region, referred to as a "local strain approximation." In this manner one could study the interaction between the electronic structure and long-wavelength acoustic phonons.

C. Tight-binding Hamiltonian with strain

Starting from the optimized lattice constant for each material under study, collected in Table II, we use DFT calculations of the electronic structure followed by a transformation to an atomiclike basis of maximally localized Wannier functions (MLWFs) [63,64] in order to determine the tight-binding parameters for a range of input strain values. By fitting the variations in the parameters as a function of u_{xx}, u_{yy}, and u_{xy}, we arrive at a complete tight-binding Hamiltonian for any choice of uniform strain. The vertical positions of the chalcogen atoms are allowed to adjust based on the isotropic strain.

A monolayer T-type TMDC has D_{3d} symmetry, which includes xz mirror symmetry, C_2 rotation symmetry about the y axis, inversion symmetry, and $\mathcal{R}_3$ rotation symmetry about the z axis. The threefold rotational symmetry of the crystal means that hopping terms to equivalent neighbor atoms will appear differently in a Hamiltonian matrix with a fixed rectangular coordinate system. However, careful choice of reference hopping vectors and analysis of the symmetry-allowed matrix elements result in significant constraints on the form of the Hamiltonian matrix.

Our model of the electronic band structure includes 11 orbitals: five d orbitals, d_{xy}, d_{yz}, $d_{x^2-y^2}$, d_{xz}, and d_{z^2} from the metal atom at the M site (origin), and three p orbitals, p_x, p_y, and p_z from each chalcogen atom, located at X_1 (upper) and X_2 (lower) sites. In what follows we use this ordering of basis orbitals to define the tight-binding Hamiltonian, including hopping terms up to third-nearest neighbor (3NN) and all dependence on isotropic and anisotropic strain, $(u_{xx} + u_{yy})$ and $(u_{xx} - u_{yy}, 2u_{xy})$, respectively.

The on-site energy represents the interactions between orbitals located at the same atom. At X_1 sites the chalcogen p-orbital on-site energy has the following form:

$$H = \begin{bmatrix} \epsilon_0 & 0 & 0 \\ 0 & \epsilon_0 & 0 \\ 0 & 0 & \epsilon_1 \end{bmatrix} + (u_{xx} + u_{yy}) \begin{bmatrix} \alpha_0^{(0)} & 0 & 0 \\ 0 & \alpha_0^{(0)} & 0 \\ 0 & 0 & \alpha_1^{(0)} \end{bmatrix} + (u_{xx} - u_{yy}) \begin{bmatrix} \beta_0^{(0)} & 0 & \beta_1^{(0)} \\ 0 & -\beta_0^{(0)} & 0 \\ \beta_1^{(0)} & 0 & 0 \end{bmatrix}$$
$$+ (2u_{xy}) \begin{bmatrix} 0 & \beta_0^{(0)} & 0 \\ \beta_0^{(0)} & 0 & -\beta_1^{(0)} \\ 0 & -\beta_1^{(0)} & 0 \end{bmatrix}. \tag{4}$$

At X_2 sites, the on-site Hamiltonian is the same as the ones at X_1 sites (including strain). At M sites the metal d-orbital on-site Hamiltonian reads

$$H = \begin{bmatrix} \epsilon_2 & \epsilon_5 & 0 & 0 & 0 \\ \epsilon_5 & \epsilon_3 & 0 & 0 & 0 \\ 0 & 0 & \epsilon_2 & -\epsilon_5 & 0 \\ 0 & 0 & -\epsilon_5 & \epsilon_3 & 0 \\ 0 & 0 & 0 & 0 & \epsilon_4 \end{bmatrix} + (u_{xx}+u_{yy}) \begin{bmatrix} \alpha_2^{(0)} & \alpha_5^{(0)} & 0 & 0 & 0 \\ \alpha_5^{(0)} & \alpha_3^{(0)} & 0 & 0 & 0 \\ 0 & 0 & \alpha_2^{(0)} & -\alpha_5^{(0)} & 0 \\ 0 & 0 & -\alpha_5^{(0)} & \alpha_3^{(0)} & 0 \\ 0 & 0 & 0 & 0 & \alpha_4^{(0)} \end{bmatrix}$$
$$+ (u_{xx}-u_{yy}) \begin{bmatrix} \beta_2^{(0)} & \beta_4^{(0)} & 0 & 0 & 0 \\ \beta_4^{(0)} & \beta_3^{(0)} & 0 & 0 & 0 \\ 0 & 0 & -\beta_2^{(0)} & \beta_4^{(0)} & \beta_5^{(0)} \\ 0 & 0 & \beta_4^{(0)} & -\beta_3^{(0)} & \beta_6^{(0)} \\ 0 & 0 & \beta_5^{(0)} & \beta_6^{(0)} & 0 \end{bmatrix} + (2u_{xy}) \begin{bmatrix} 0 & 0 & \beta_2^{(0)} & -\beta_4^{(0)} & \beta_5^{(0)} \\ 0 & 0 & \beta_4^{(0)} & -\beta_3^{(0)} & -\beta_6^{(0)} \\ \beta_2^{(0)} & \beta_4^{(0)} & 0 & 0 & 0 \\ -\beta_4^{(0)} & -\beta_3^{(0)} & 0 & 0 & 0 \\ \beta_5^{(0)} & -\beta_6^{(0)} & 0 & 0 & 0 \end{bmatrix}. \quad (5)$$

Each atom has six nearest neighbors (1NN), three from each of the other two sites. There are three types of first-neighbor interactions: (X_1-M), (X_2-M), and (X_2-X_1). For the (X_1-M) interaction we take as a reference bond the hopping from M at the origin to X_1 at $(\boldsymbol{a}_1+\boldsymbol{a}_2)/3$. The corresponding Hamiltonian is

$$H = \begin{bmatrix} 0 & 0 & t_0^{(1)} & t_1^{(1)} & t_2^{(1)} \\ t_3^{(1)} & t_4^{(1)} & 0 & 0 & 0 \\ 0 & 0 & t_5^{(1)} & t_6^{(1)} & t_7^{(1)} \end{bmatrix} + (u_{xx}+u_{yy}) \begin{bmatrix} 0 & 0 & \alpha_0^{(1)} & \alpha_1^{(1)} & \alpha_2^{(1)} \\ \alpha_3^{(1)} & \alpha_4^{(1)} & 0 & 0 & 0 \\ 0 & 0 & \alpha_5^{(1)} & \alpha_6^{(1)} & \alpha_7^{(1)} \end{bmatrix}$$
$$+ (u_{xx}-u_{yy}) \begin{bmatrix} 0 & 0 & \beta_0^{(1)} & \beta_1^{(1)} & \beta_2^{(1)} \\ \beta_3^{(1)} & \beta_4^{(1)} & 0 & 0 & 0 \\ 0 & 0 & \beta_5^{(1)} & \beta_6^{(1)} & \beta_7^{(1)} \end{bmatrix} + (2u_{xy}) \begin{bmatrix} \beta_8^{(1)} & \beta_9^{(1)} & 0 & 0 & 0 \\ 0 & 0 & \beta_{10}^{(1)} & \beta_{11}^{(1)} & \beta_{12}^{(1)} \\ \beta_{13}^{(1)} & \beta_{14}^{(1)} & 0 & 0 & 0 \end{bmatrix}. \quad (6)$$

For the (X_2-M) interaction, with the hopping from M at the origin to X_2 at $-(\boldsymbol{a}_1+\boldsymbol{a}_2)/3$ taken as the reference, the Hamiltonian has the same form as (X_1-M) with an overall (-1) factor. The final first-neighbor coupling, (X_2-X_1), with reference bond chosen along the positive x axis, has the form

$$H = \begin{bmatrix} t_8^{(1)} & 0 & t_{11}^{(1)} \\ 0 & t_9^{(1)} & 0 \\ t_{11}^{(1)} & 0 & t_{10}^{(1)} \end{bmatrix} + (u_{xx}+u_{yy}) \begin{bmatrix} \alpha_8^{(1)} & 0 & \alpha_{11}^{(1)} \\ 0 & \alpha_9^{(1)} & 0 \\ \alpha_{11}^{(1)} & 0 & \alpha_{10}^{(1)} \end{bmatrix}$$
$$+ (u_{xx}-u_{yy}) \begin{bmatrix} \beta_{15}^{(1)} & 0 & \beta_{18}^{(1)} \\ 0 & \beta_{16}^{(1)} & 0 \\ \beta_{18}^{(1)} & 0 & \beta_{17}^{(1)} \end{bmatrix} + (2u_{xy}) \begin{bmatrix} 0 & \beta_{19}^{(1)} & 0 \\ \beta_{19}^{(1)} & 0 & \beta_{20}^{(1)} \\ 0 & \beta_{20}^{(1)} & 0 \end{bmatrix}. \quad (7)$$

Each atom has six second-nearest neighbors (2NN) of the same type. In each case the reference bond is along the positive y axis. The (X_1-X_1) coupling has the form

$$H = \begin{bmatrix} t_0^{(2)} & t_3^{(2)} & t_4^{(2)} \\ -t_3^{(2)} & t_1^{(2)} & t_5^{(2)} \\ t_4^{(2)} & -t_5^{(2)} & t_2^{(2)} \end{bmatrix} + (u_{xx}+u_{yy}) \begin{bmatrix} \alpha_0^{(2)} & \alpha_3^{(2)} & \alpha_4^{(2)} \\ -\alpha_3^{(2)} & \alpha_1^{(2)} & \alpha_5^{(2)} \\ \alpha_4^{(2)} & -\alpha_5^{(2)} & \alpha_2^{(2)} \end{bmatrix}$$
$$+ (u_{xx}-u_{yy}) \begin{bmatrix} \beta_0^{(2)} & \beta_3^{(2)} & \beta_4^{(2)} \\ -\beta_3^{(2)} & \beta_1^{(2)} & \beta_5^{(2)} \\ \beta_4^{(2)} & -\beta_5^{(2)} & \beta_2^{(2)} \end{bmatrix} + (2u_{xy}) \begin{bmatrix} 0 & \beta_6^{(2)} & \beta_7^{(2)} \\ \beta_6^{(2)} & 0 & \beta_8^{(2)} \\ -\beta_7^{(2)} & \beta_8^{(2)} & 0 \end{bmatrix}, \quad (8)$$

while the (X_2-X_2) interaction has some (-1) phase factors compared to (X_1-X_1), as shown:

$$H = \begin{bmatrix} t_0^{(2)} & -t_3^{(2)} & t_4^{(2)} \\ t_3^{(2)} & t_1^{(2)} & -t_5^{(2)} \\ t_4^{(2)} & t_5^{(2)} & t_2^{(2)} \end{bmatrix} + (u_{xx}+u_{yy}) \begin{bmatrix} \alpha_0^{(2)} & -\alpha_3^{(2)} & \alpha_4^{(2)} \\ \alpha_3^{(2)} & \alpha_1^{(2)} & -\alpha_5^{(2)} \\ \alpha_4^{(2)} & \alpha_5^{(2)} & \alpha_2^{(2)} \end{bmatrix}$$
$$+ (u_{xx}-u_{yy}) \begin{bmatrix} \beta_0^{(2)} & -\beta_3^{(2)} & \beta_4^{(2)} \\ \beta_3^{(2)} & \beta_1^{(2)} & -\beta_5^{(2)} \\ \beta_4^{(2)} & \beta_5^{(2)} & \beta_2^{(2)} \end{bmatrix} + (2u_{xy}) \begin{bmatrix} 0 & \beta_6^{(2)} & -\beta_7^{(2)} \\ \beta_6^{(2)} & 0 & \beta_8^{(2)} \\ \beta_7^{(2)} & \beta_8^{(2)} & 0 \end{bmatrix}. \tag{9}$$

The Hamiltonian for the (M-M) interaction has the form

$$H = \begin{bmatrix} t_6^{(2)} & t_{11}^{(2)} & 0 & 0 & 0 \\ t_{11}^{(2)} & t_7^{(2)} & 0 & 0 & 0 \\ 0 & 0 & t_8^{(2)} & t_{12}^{(2)} & t_{13}^{(2)} \\ 0 & 0 & t_{12}^{(2)} & t_9^{(2)} & t_{14}^{(2)} \\ 0 & 0 & t_{13}^{(2)} & t_{14}^{(2)} & t_{10}^{(2)} \end{bmatrix} + (u_{xx}+u_{yy}) \begin{bmatrix} \alpha_6^{(2)} & \alpha_{11}^{(2)} & 0 & 0 & 0 \\ \alpha_{11}^{(2)} & \alpha_7^{(2)} & 0 & 0 & 0 \\ 0 & 0 & \alpha_8^{(2)} & \alpha_{12}^{(2)} & \alpha_{13}^{(2)} \\ 0 & 0 & \alpha_{12}^{(2)} & \alpha_9^{(2)} & \alpha_{14}^{(2)} \\ 0 & 0 & \alpha_{13}^{(2)} & \alpha_{14}^{(2)} & \alpha_{10}^{(2)} \end{bmatrix}$$
$$+ (u_{xx}-u_{yy}) \begin{bmatrix} \beta_9^{(2)} & \beta_{14}^{(2)} & 0 & 0 & 0 \\ \beta_{14}^{(2)} & \beta_{10}^{(2)} & 0 & 0 & 0 \\ 0 & 0 & \beta_{11}^{(2)} & \beta_{15}^{(2)} & \beta_{16}^{(2)} \\ 0 & 0 & \beta_{15}^{(2)} & \beta_{12}^{(2)} & \beta_{17}^{(2)} \\ 0 & 0 & \beta_{16}^{(2)} & \beta_{17}^{(2)} & \beta_{13}^{(2)} \end{bmatrix} + (2u_{xy}) \begin{bmatrix} 0 & 0 & \beta_{18}^{(2)} & \beta_{19}^{(2)} & \beta_{20}^{(2)} \\ 0 & 0 & \beta_{21}^{(2)} & \beta_{22}^{(2)} & \beta_{23}^{(2)} \\ \beta_{18}^{(2)} & \beta_{21}^{(2)} & 0 & 0 & 0 \\ \beta_{19}^{(2)} & \beta_{22}^{(2)} & 0 & 0 & 0 \\ \beta_{20}^{(2)} & \beta_{23}^{(2)} & 0 & 0 & 0 \end{bmatrix}. \tag{10}$$

Similar to first-neighbor coupling, each atom has three third-nearest neighbors (3NN) of each of the other two types, but with different reference bonds. The (X_1-M) interaction, with reference bond pointing from the origin to $-2(\boldsymbol{a}_1+\boldsymbol{a}_2)/3$, takes the form

$$H = \begin{bmatrix} 0 & 0 & t_0^{(3)} & t_1^{(3)} & t_2^{(3)} \\ t_3^{(3)} & t_4^{(3)} & 0 & 0 & 0 \\ 0 & 0 & t_5^{(3)} & t_6^{(3)} & t_7^{(3)} \end{bmatrix} + (u_{xx}+u_{yy}) \begin{bmatrix} 0 & 0 & \alpha_0^{(3)} & \alpha_1^{(3)} & \alpha_2^{(3)} \\ \alpha_3^{(3)} & \alpha_4^{(3)} & 0 & 0 & 0 \\ 0 & 0 & \alpha_5^{(3)} & \alpha_6^{(3)} & \alpha_7^{(3)} \end{bmatrix}$$
$$+ (u_{xx}-u_{yy}) \begin{bmatrix} 0 & 0 & \beta_0^{(3)} & \beta_1^{(3)} & \beta_2^{(3)} \\ \beta_3^{(3)} & \beta_4^{(3)} & 0 & 0 & 0 \\ 0 & 0 & \beta_5^{(3)} & \beta_6^{(3)} & \beta_7^{(3)} \end{bmatrix} + (2u_{xy}) \begin{bmatrix} \beta_8^{(3)} & \beta_9^{(3)} & 0 & 0 & 0 \\ 0 & 0 & \beta_{10}^{(3)} & \beta_{11}^{(3)} & \beta_{12}^{(3)} \\ \beta_{13}^{(3)} & \beta_{14}^{(3)} & 0 & 0 & 0 \end{bmatrix}. \tag{11}$$

The (X_2-M) interaction, with reference bond from the origin to $2(\boldsymbol{a}_1+\boldsymbol{a}_2)/3$, has the same form as the above with an overall (-1) factor. Finally, the (X_2-X_1) coupling has a reference vector $-2(\boldsymbol{a}_1+\boldsymbol{a}_2)/3$, and the Hamiltonian takes the form

$$H = \begin{bmatrix} t_8^{(3)} & 0 & t_{11}^{(3)} \\ 0 & t_9^{(3)} & 0 \\ t_{11}^{(3)} & 0 & t_{10}^{(3)} \end{bmatrix} + (u_{xx}+u_{yy}) \begin{bmatrix} \alpha_8^{(3)} & 0 & \alpha_{11}^{(3)} \\ 0 & \alpha_9^{(3)} & 0 \\ \alpha_{11}^{(3)} & 0 & \alpha_{10}^{(3)} \end{bmatrix} + (u_{xx}-u_{yy}) \begin{bmatrix} \beta_{15}^{(3)} & 0 & \beta_{18}^{(3)} \\ 0 & \beta_{16}^{(3)} & 0 \\ \beta_{18}^{(3)} & 0 & \beta_{17}^{(3)} \end{bmatrix} + (2u_{xy}) \begin{bmatrix} 0 & \beta_{19}^{(3)} & 0 \\ \beta_{19}^{(3)} & 0 & \beta_{20}^{(3)} \\ 0 & \beta_{20}^{(3)} & 0 \end{bmatrix}. \tag{12}$$

For each of the above couplings in Eqs. (6)–(12) there are two additional symmetrically equivalent couplings related by $2\pi/3$ rotations (clockwise and counterclockwise). In order to implement these rotations on the tight-binding Hamiltonian, we use the following unitary transformations with $\phi = 2\pi/3$ to implement the counterclockwise rotation on p and d subspaces, respectively:

$$\mathcal{U}^X(\phi) = \begin{bmatrix} \cos\phi & \sin\phi & 0 \\ -\sin\phi & \cos\phi & 0 \\ 0 & 0 & 1 \end{bmatrix}, \tag{13}$$

$$\mathcal{U}^M(\phi) = \begin{bmatrix} \cos 2\phi & 0 & -\sin 2\phi & 0 & 0 \\ 0 & \cos\phi & 0 & -\sin\phi & 0 \\ \sin 2\phi & 0 & \cos 2\phi & 0 & 0 \\ 0 & \sin\phi & 0 & \cos\phi & 0 \\ & 0 & 0 & 0 & 1 \end{bmatrix}. \tag{14}$$

Note that the orbital subspaces rotate in the opposite direction from the coordinate axes. The 2NN couplings each have three additional symmetrically equivalent couplings related by a mirror symmetry in the xz plane.

TABLE II. Calculated equilibrium lattice constant, a (Å), for the TMDC MX_2.

M \ X	S	Se	Te
Ti	3.41	3.53	3.74
Nb	3.35	3.46	3.62
Ta	3.36	3.49	3.64

The strain-dependent tight-binding Hamiltonian for each material is specified by 163 parameters, which is significantly fewer than the 1056 parameters in a generic 11-dimensional Hamiltonian with isotropic and anisotropic strain dependence. Furthermore, these parameters are all extracted directly from the Wannier transformation of the DFT results (averaging over symmetrically equivalent terms) and are not the result of any fitting to the band structure. The parameters for each material are tabulated in the Appendix.

D. Work function

The work function for each material is the difference in energy between the Fermi level of the TMDC and the vacuum (a location far from the TMDC layer): $\Delta\Phi = E_{\rm vac} - E_{\rm F}$. This can be easily extracted from the DFT total potential for each value of isotropic strain, and shows a mild (few percent) dependence on the strain, which can affect the diagonal ϵ values as well as the $\alpha^{(0)}$ couplings. The values reported in the tables in the Appendix have the strain-dependent work function subtracted from the on-site couplings before fitting. The work function for the unstrained materials, which decreases with increasing atomic number of both the metal and the chalcogen atoms, is included in Table I.

E. Spin-orbit coupling

Atomic spin-orbit coupling (SOC) is described by the Hamiltonian $H_{\rm soc} = \lambda_{\rm soc} \boldsymbol{L} \cdot \boldsymbol{S}$. We can extract the value of $\lambda_{\rm soc}$ for each atomic species by considering the splitting between valence states in a single atom as calculated by DFT. Assuming the wave functions are eigenstates of $\boldsymbol{J}$, $\boldsymbol{L}$, and $\boldsymbol{S}$, the energy splitting is given by the difference between $j = \ell + 1/2$ and $j = \ell - 1/2$ states, namely, $\Delta E_{\rm soc} = \lambda_{\rm soc}(\ell + 1/2)$. The value of $\lambda_{\rm soc}$, in units of eV, is shown in Table III for the six species considered here.

TABLE III. The atomic spin-orbit-coupling strength $\lambda_{\rm soc}$, in units of eV.

	Ti	Nb	Ta	S	Se	Te
$\lambda_{\rm soc}$ (eV)	0.018	0.071	0.232	0.056	0.247	0.512

IV. MODEL VALIDATION

In this section we demonstrate the accuracy with which our strain-dependent TBH reproduces the DFT band structures. Figure 3(a) shows that the band structure near the Fermi energy is captured by the 11-band Wannier transformation, because the bands calculated with DFT and those reconstructed from the full basis of Wannier functions show virtually no differences.

Our tight-binding model, however, ignores interactions beyond 3NN, and it is important to examine the extent to which neglecting those longer-range couplings affects the band structure. Figure 3(b) shows the 3NN TBH band structure along with the full Wannier reconstruction and a fifth-nearest-neighbor (5NN) truncation. The qualitative band structures agree well, and the most significant quantitative differences appear in bands far from the Fermi level. These differences arise from the overlap with orbitals that are not included in our 11-band model. The Wannierization procedure used to calculate the MLWF includes the effects from these other states as longer-range hopping terms, beyond even 5NN.

In Fig. 4, we show the effect of 2% isotropic compression and expansion on the band structure of $TaSe_2$. The black bands are the result of DFT calculations and the red bands are from our 3NN tight-binding model, demonstrating that our model tracks the decrease in band dispersion as the crystal is

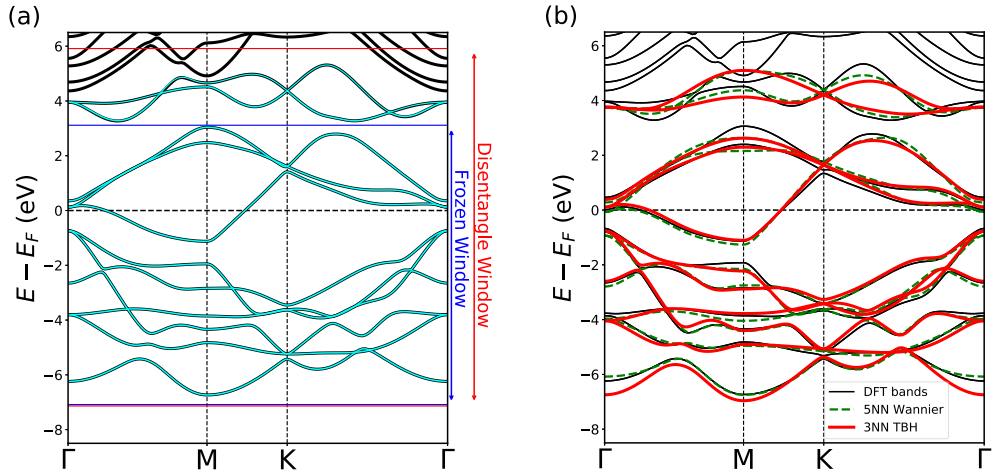

FIG. 3. (a) Comparison of the band structure calculated with DFT (black) and the full Wannier basis (cyan) for unstrained TaS_2. Also shown are the energy windows used to define the Wannier transformation and disentangle the bands arising from other orbitals [62,64]. (b) Comparison of the band structure computed directly with DFT (thin black), 5NN Wannier basis (dashed green), and the 3NN TBH parametrization (thick red) for unstrained TaS_2.

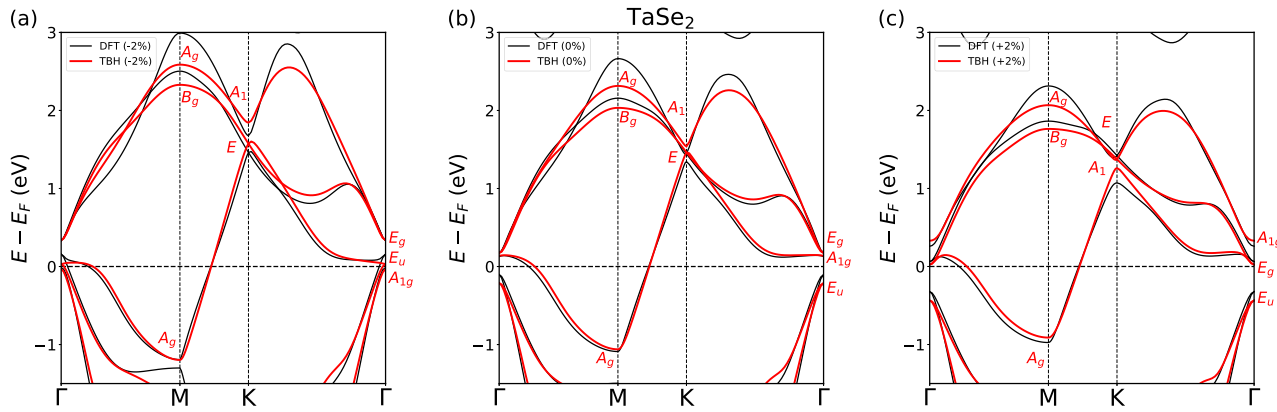

FIG. 4. Comparison of the band structure calculated using the 3NN TBH (red) and DFT (black) for a $TaSe_2$ crystal with three values of isotropic strain: (a) 2% compression, (b) unstrained, and (c) 2% expansion. The TBH bands are labeled by the irreducible representation of the symmetry group of the wave vector at each high-symmetry point. (Γ: D_{3d}, M: C_{2h}, K: D_3).

expanded. From the tight-binding Hamiltonian it is easy to determine the irreducible representations of each band at the high-symmetry points, Γ, M, and K (see Fig. 4). Changing the lattice constant from 2% compression to 2% expansion results in the reordering of representations at the Γ point near E_F, with the A_{1g} singlet rising up through first the E_u doublet (at the equilibrium lattice constant) and then the E_g doublet (at 2% expansion). This reordering is accurately captured by the tight-binding model. However, the band reordering at the K point caused by lattice expansion, with the singlet A_1 sinking below the E doublet, has already occurred in the DFT at the equilibrium lattice constant, whereas it requires a slight expansion in the lattice before it occurs in the tight-binding model.

We can also compare the TBH with the addition of atomic spin-orbit coupling to the DFT results. Specifically, we consider the three bands in $TaSe_2$ that lie just above E_F at Γ in the unstrained crystal. Figure 5 shows the change in energy as calculated within DFT (black) or using the tight-binding parametrization including atomic SOC: there is good quantitative agreement between the two approaches.

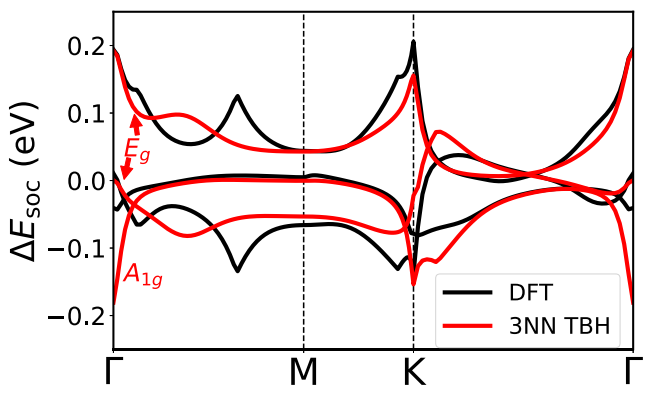

FIG. 5. Change in band energy due to spin-orbit coupling for three bands near the Fermi level in unstrained $TaSe_2$. These bands can be identified as an A_{1g} singlet and E_g doublet at Γ. The difference in DFT calculated band energies with and without SOC, $\Delta E_{\rm soc} = E_{\rm with-soc} - E_{\rm no-soc}$, is shown in black, whereas the differences in tight-binding eigenvalues with and without SOC is shown in red.

V. APPLICATIONS

There are many proposals for strain engineering of 2D materials. A 2D pattern of artificial atoms has been generated by draping a single layer of MoS_2 over a periodic array of nanocones in a substrate, creating regions of higher and lower biaxial strain [65]. More recently, draping a graphene sheet over a step edge in a copper substrate has been shown to produce one-dimensional (1D) ripples along the direction of the step edge [66]. Such a 1D ripple is also essentially a snapshot of a longitudinal acoustic (LA) phonon. Lattice distortions also occur spontaneously in systems that undergo CDW reconstructions. Though these generally occur over much shorter length scales, for small distortions our strain model should be able to capture the most important effects. We demonstrate the usefulness and limitations of our strain-dependent tight-binding model for systems with nonuniform strain patterns by applying it to three example structures: a 1D sinusoidal ripple in TaS_2, the 2×2 CDW in $TiSe_2$, and the $\sqrt{13} \times \sqrt{13}$ CDW in TaS_2.

A. One-dimensional rippling

We have modeled the effects of long-wavelength lattice distortions on the electronic structure of TaS_2 subject to a sinusoidal strain of variable amplitude and wavelength in the x direction. Our model accounts only for in-plane lattice distortions, which were shown to be important in reproducing the experimental data in Ref. [66]. Our treatment here does not consider out-of-plane displacements beyond the vertical relaxation of the chalcogen atoms.

To model a nonuniform strain pattern, we first create an atomic supercell that is large enough to include the entire periodic strain pattern. For the 1D ripple, we use a rectangular unit cell containing two formula units of TaS_2, and repeat it N times in the x direction, as shown schematically in Fig. 6(a) for $N = 4$. Our model includes up to 3NN hopping, so each atom in the supercell interacts with 18 other atoms in addition to the on-site interaction. For each "bond" between interacting atoms we calculate the matrix elements in the Hamiltonian using our tight-binding parametrization with the components of the strain field evaluated at the center of the bond. This approximation ensures that the model Hamiltonian remains Hermitian. For the 1D ripple the displacement field is $u(r) =$

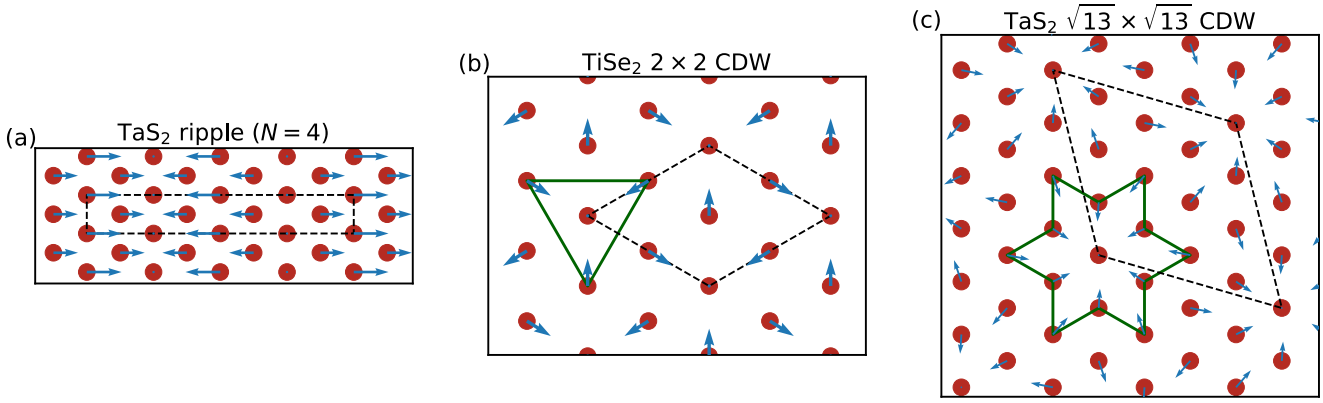

FIG. 6. The displacements of the metal atoms used in the applications of the strain-dependent TBH. (a) Sinusoidal strain in the x direction with a period of $N = 4$ rectangular units. (b) 2×2 CDW pattern for $TiSe_2$. (c) $\sqrt{13} \times \sqrt{13}$ CDW pattern for TaS_2. The supercells are shown with dashed black lines, and the chalcogen atoms are omitted for clarity.

$A \sin(2\pi x/a\sqrt{3}N)\hat{x}$ and thus $u_{xx} = B\cos(2\pi x/a\sqrt{3}N)$ and $u_{yy} = u_{xy} = u_{yx} = 0$.

The supercell geometry and consequent folded band structure complicate the interpretation of the electronic structure. In this example our ripple has $2 \times 11 \times N$ bands. One way to make connections with the simpler pristine crystal band structure is through an "unfolding procedure" to obtain the "effective band structure." This method has been established to interpret the perturbations to the pristine band structure due to the presence of impurities, disordered alloys, and structural reconstructions in DFT calculations that use a supercell geometry [67–70]. The effective band structure can be further compared with the band structure derived from ARPES.

In practice, the unfolding procedure is carried out with the proper crystal momentum projection based on the pristine unit cell, where the corresponding Fourier component determines the unfolding weight. Figure 7 shows the unfolded band structures for an $N = 4$ TaS_2 supercell both with and without the 1D sinusoidal strain. For comparison, we studied a supercell with displaced atoms directly using DFT, followed by the Wannier transformation and unfolding of the supercell band structure, and found only small differences. While in this case the DFT + Wannier calculation is not computationally prohibitive, it still takes several hours of CPU time for each configuration, and the resources required grow with the size of the supercell. By contrast, once the framework of the TBH supercell has been set up, the unfolded band structure can be produced much faster for any chosen amplitude or wavelength of the strain pattern, and for any of the nine T-type TMDC materials we have modeled. Increasing the wavelength of the strain pattern to $\lambda = 93$ Å ($N = 16$) results in a supercell with 96 atoms, which makes the DFT calculation very computationally demanding, while the TBH result, shown in Fig. 7(c), is obtained in under 1 min using a laptop computer.

The preceding example can be viewed as a static structure produced by draping a monolayer TMDC over a step edge, or it can be viewed as a snapshot of a LA phonon. Viewed in this latter sense, the energy splittings in the distorted band structures in Fig. 7 show that the LA phonon couples most strongly to the electrons in the valence band near Γ and in the conduction band at M and Q (located partway between K and Γ), with a similar magnitude for phonon momentum $q = (2\pi/23)$ Å^{-1} and $q = (2\pi/93)$ Å^{-1}.

In T-TMDCs, CDW order is prevalent and affects the underlying electronic properties. Compared to the pristine crystal structure, the CDW order and electron-phonon couplings cause deformed and reconstructed atomic positions. For example, the T-$TiSe_2$ crystal exhibits a 2×2 reconstruction, while the T-TaS_2 crystal shows so-called Star-of-David deformations in the commensurate CDW phase with a $\sqrt{13} \times \sqrt{13}$ supercell. Though our TBH model is most applicable to the preceding example of long-wavelength LA phonons, it is interesting to test the limits of its validity. It is in this spirit that we apply our model to CDW distortions in the following two sections.

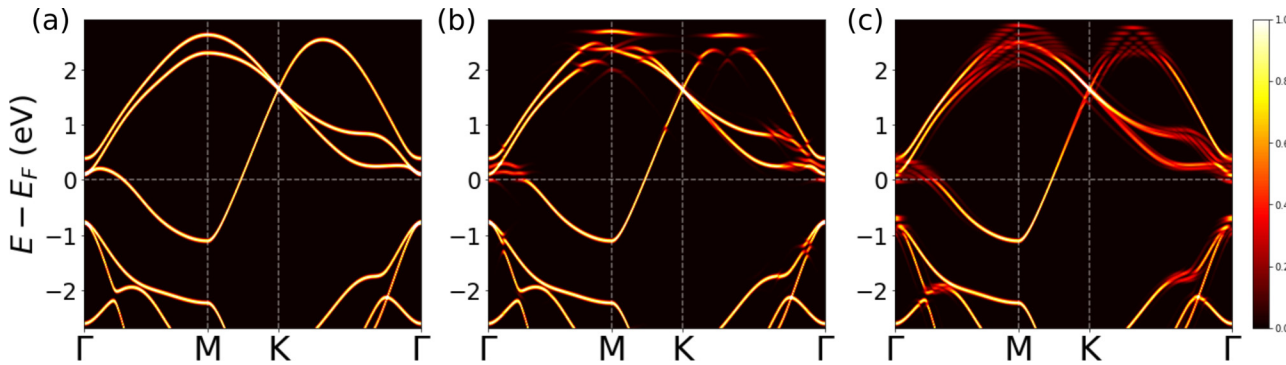

FIG. 7. Band structures for an $N \times 1$ rectangular supercell of TaS_2, unfolded to a path in the Brillouin zone of the three-atom primitive unit cell. (a) TBH bands for $N = 4$ without strain. (b) TBH bands for $N = 4$ subject to 1D sinusoidal strain with amplitude $B = 0.02$ and wavelength $\lambda = 23$ Å. (c) TBH bands for $N = 16$, subject to 1D sinusoidal strain with amplitude $B = 0.02$ and wavelength $\lambda = 93$ Å.

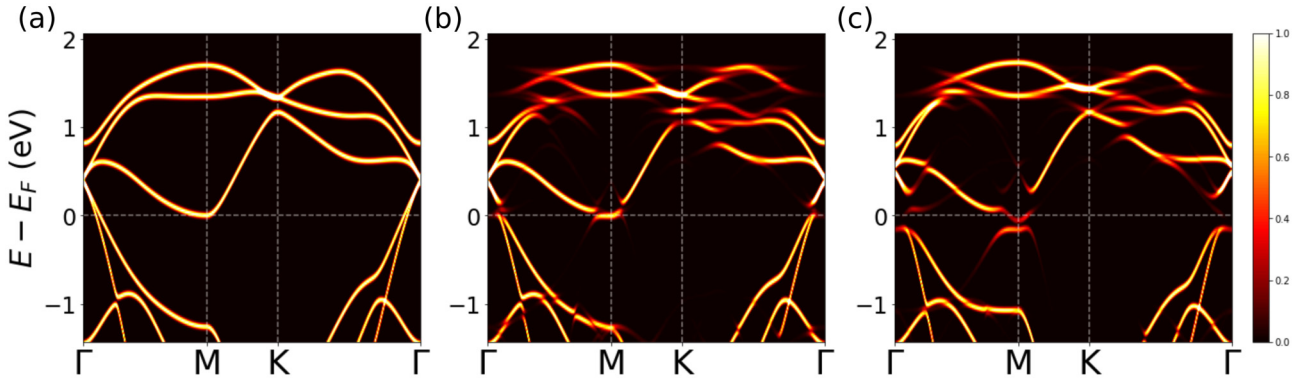

FIG. 8. Band structures for the 2×2 CDW supercell of $TiSe_2$, unfolded to a path in the Brillouin zone of the three-atom primitive unit cell. (a) TBH bands without the CDW distortion. (b) TBH bands for a strain pattern fit to the CDW displacements calculated with DFT. (c) DFT band structure for the relaxed CDW, for comparison.

B. $TiSe_2$ CDW

Starting from the known 2×2 CDW pattern in $TiSe_2$, we expand the continuous displacement field in terms of the Fourier components of the first shell of reciprocal lattice vectors and fit to the positions of the Ti atoms in the 2×2 supercell. The derivative of this displacement field is then used to determine the components of the strain field at the center of each bond between interacting atoms in the 2×2 supercell. Unlike the case of the 1D ripple, the $TiSe_2$ CDW strain pattern includes a nonzero antisymmetric scalar, ω_{xy}, which represents a local rotation. This is implemented in the TBH by rotating the strain-independent piece of the Hamiltonian for each bond by an angle $\phi = \omega_{xy}(x, y)$ evaluated at the center of each bond, using the matrices of Eqs. (13) and (14).

The CDW pattern could be taken from experimental measurements, but here we generate it using DFT in order to also have a reference against which to compare our tight-binding model. We first build a 2×2 supercell, perturb the Ti atoms slightly, and use DFT to relax the positions of all atoms. The CDW indeed develops, with changes in the distances between the Ti atoms of ± 0.08 Å, which is 2.3% of the optimized DFT lattice constant of 3.53 Å. This amount of strain is at the upper limit of the uniform strain which we used to extract the parameters of the strain-dependent TBH and where the response in the TBH parameters was still quite linear. A schematic of the metal atom displacements is shown in Fig. 6(b).

Figure 8 shows the pristine and CDW-strained $TiSe_2$ bands unfolded to the primitive cell Brillouin zone. The opening of small gaps at the Fermi level is clearly captured, though underestimated, and the unfolded bands reproduce most of the qualitative features found in the unfolded bands calculated directly with DFT + Wannier, shown in Fig. 8(c).

C. TaS_2 CDW

The simple, symmetric model we have developed reveals its limitations when applied to the $\sqrt{13} \times \sqrt{13}$ CDW pattern that occurs in TaS_2 and $TaSe_2$. For the former, relaxation of the supercell using DFT yields the experimentally observed CDW pattern, shown schematically in Fig. 6(c). The nearest Ta-Ta distances can increase by as much as 0.43 Å while other distances decrease by up to 0.2 Å, a range of -6% to $+13\%$ of the 3.36 Å lattice constant. Displacements this large might be expected to exceed the linear strain regime parametrized in our model. Indeed, calculations using larger isotropic strains show that the response of one of the 1NN Ta-S couplings becomes very nonlinear, as shown in Fig. 9. Using the strain-dependent TBH to compute the electronic structure for the TaS_2 CDW in the same manner as for $TiSe_2$, including local rotation ω and taking the strain field from a fit to the Ta positions in the relaxed DFT CDW structure, we see in Fig. 10 that many of the smaller features in the unfolded CDW band structure are well reproduced. However, the TBH model fails to capture the significant flat band that emerges at Γ and is clearly visible in the DFT calculation, Fig. 10(c). Using a simpler empirical tight-binding model, Rossnagel and Smith were able to reproduce the flat band, but only when including both the structural distortion and spin-orbit coupling [71]. Our DFT calculations of the CDW capture this flat band even without spin-orbit coupling, demonstrating the subtlety of this feature. In this case the perturbation from the pristine T structure is so large that nonlinear effects in the strain response become important. The same is true for distorted phases such as the T' structure (which has a dimerization of metal atoms in one direction). This is not a breakdown of

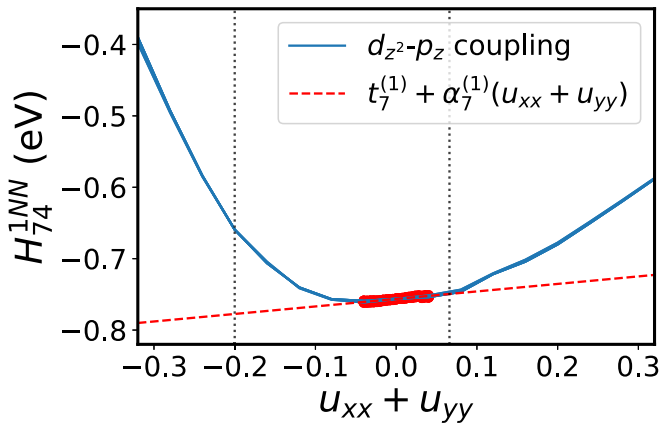

FIG. 9. Magnitude of the 1NN matrix element H_{74}^{1NN}, namely, the d_{z^2}-p_z coupling in TaS_2, as a function of isotropic strain, $u_{xx} + u_{yy}$. The red points represent strain in the range $\pm 2\%$ used to produce the linear parametrization (red dashed line) for the strain-dependent TBH. The vertical dotted black lines indicate the range of isotropic strain occurring in the TaS_2 CDW pattern.

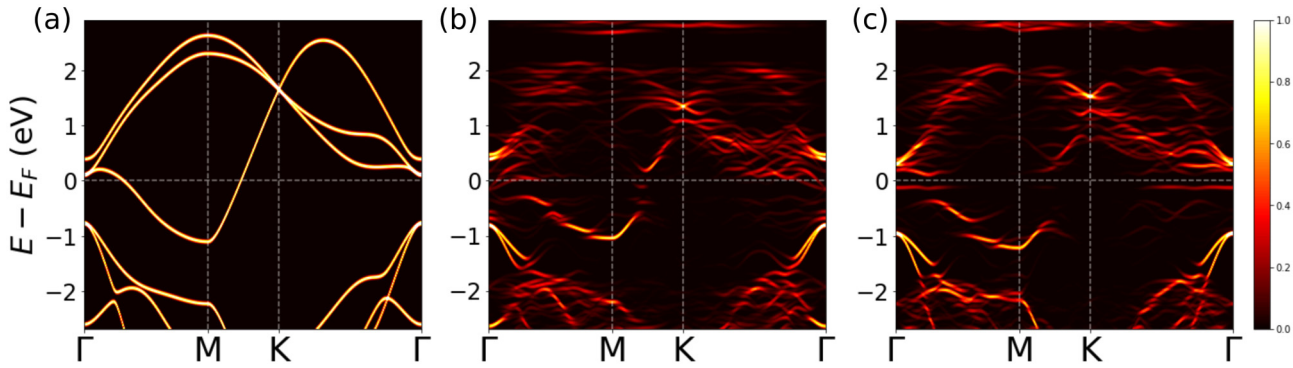

FIG. 10. Band structures for the $\sqrt{13} \times \sqrt{13}$ CDW supercell of TaS_2, unfolded to a path in the Brillouin zone of the three-atom primitive unit cell. (a) TBH bands without the CDW distortion, (b) TBH bands for a strain pattern fit to the CDW displacements calculated with DFT, and (c) DFT band structure for the relaxed CDW.

the underlying procedure, for one can still use the Wannier transformation of the DFT results to construct accurate tight-binding models to study the coupling to acoustic phonons. However, the complexity increases significantly, preventing us from writing simple, symmetric models. Because the tight-binding model by itself does not provide information about the spatial properties of the orbitals, one would need to go back to the Wannier functions in order to learn about the orbital structure, which has been shown to change depending on the stacking order in the CDW phase of bulk TaS_2 [10]. In addition, because our model is based on DFT, it does not account for electron correlation effects.

VI. CONCLUSION

We have used the Wannier transformation of plane-wave DFT calculations to construct precise, strain-dependent tight-binding Hamiltonians for group-IV and group-V TMDCs that adopt the T structure. We have further augmented the models with on-site spin-orbit-coupling terms and determined the work function for each material, providing a simple parametrization of the interaction of the electronic structure with long-wavelength acoustic phonons, which induce deformations of the primitive vectors of the structural unit cell. Moreover, we have pushed the model to the edge of its validity, applying it to short-wavelength CDW distortions. The effects of such perturbations are visualized through the technique of band-structure unfolding, revealing that the TBH model reproduces some, but not all, of the electronic features captured using DFT. This same approach could be generalized to model crystals with internal atomic displacements due to optical phonons.

From a broader perspective, the strain response of single layers is a necessary ingredient for the construction of models of van der Waals heterostructures with multiple layers. These material systems have attracted attention recently since the discovery of unconventional correlated insulating and superconducting states in magic-angle twisted bilayer graphene [72–74]. In terms of its electronic structure modeling, the layer deformation and strain from the mechanical relaxations in a twisted bilayer are shown to be relevant in modifying the electronic structure when compared with experimental observations [75]. Our modeling of single layers with strain paves the way for investigating heterostructures involving diverse types of T TMDCs and the interplay between different order parameters. The challenges in describing short-range effects indicates that for a quantitatively accurate model of a system with a CDW one would, at the very least, need to add in nonlinear strain contributions. Alternatively, one might try to use the full Wannier basis and interpolate between sampled configurations. The other crucial ingredient necessary for a comprehensive, single-particle model of the electronic structure is the proper interlayer couplings between orbitals in adjacent layers [10,76,77]. This is highlighted by the significant effect of stacking order in multilayer TaS_2 [23–25]. Modeling these interlayer couplings will be the subject of future work.

ACKNOWLEDGMENTS

We thank Stephen Carr, Jhih-Shih You, Dennis Huang, and Philip Kim for useful discussions. This work was supported by the STC Center for Integrated Quantum Materials, NSF Grant No. DMR-1231319 and by ARO MURI Award No. W911NF-14-0247. S.F. is supported by a Rutgers Center for Material Theory Distinguished Postdoctoral Fellowship. S.B.T. and J.C. recognize the support of the DOE Computational Science Graduate Fellowship (CSGF) under Grant No. DE-FG02-97ER25308. This work used the Stampede2 supercomputer at the Texas Advanced Computing Center through allocation TG-DMR120073, which is part of the Extreme Science and Engineering Discovery Environment (XSEDE), supported by NSF Grant No. ACI-1548562. We also used the Odyssey cluster supported by the FAS Division of Science, Research Computing Group at Harvard University.

APPENDIX: *T*-TMDC STRAIN-DEPENDENT TIGHT-BINDING PARAMETERS

Tables IV–X contain tight-binding parameters for each of the 9 TMDCs explicitly modeled in this study.

TABLE IV. T-type TMDC on-site strain terms in units of eV.

	TiS_2	$TiSe_2$	$TiTe_2$	NbS_2	$NbSe_2$	$NbTe_2$	TaS_2	$TaSe_2$	$TaTe_2$
ϵ_0	−10.093	−9.195	−7.117	−9.023	−8.126	−6.178	−9.444	−8.582	−6.595
ϵ_1	−10.030	−9.238	−7.324	−9.120	−8.322	−6.582	−9.532	−8.767	−7.041
ϵ_2	−7.441	−6.809	−5.080	−6.523	−5.950	−4.413	−6.374	−5.906	−4.443
ϵ_3	−7.072	−6.468	−4.776	−5.725	−5.256	−3.855	−5.375	−5.034	−3.706
ϵ_4	−7.676	−6.998	−5.269	−6.803	−6.192	−4.694	−6.700	−6.197	−4.753
ϵ_5	−0.442	−0.359	−0.304	−0.680	−0.548	−0.459	−0.779	−0.636	−0.511
$\alpha_0^{(0)}$	−5.791	−5.989	−7.350	−5.618	−4.835	−6.604	−5.162	−5.132	−4.924
$\alpha_1^{(0)}$	−3.771	−3.816	−4.825	−4.046	−3.126	−4.564	−3.080	−2.837	−2.251
$\alpha_2^{(0)}$	−6.723	−6.992	−8.206	−5.086	−4.600	−6.592	−4.074	−4.568	−4.210
$\alpha_3^{(0)}$	−8.008	−8.008	−8.649	−6.718	−5.818	−6.767	−6.918	−6.695	−5.945
$\alpha_4^{(0)}$	−6.659	−6.855	−7.738	−4.898	−4.406	−5.744	−4.175	−4.368	−4.199
$\alpha_5^{(0)}$	0.408	0.301	0.196	0.245	0.137	0.130	−0.052	−0.052	−0.275
$\beta_0^{(0)}$	−0.642	−0.604	−0.692	−0.477	−0.423	−0.589	−0.045	−0.033	−0.349
$\beta_1^{(0)}$	0.410	0.505	0.594	0.355	0.553	0.715	1.164	1.360	1.262
$\beta_2^{(0)}$	0.476	0.367	0.251	0.576	0.445	0.342	0.403	0.255	0.096
$\beta_3^{(0)}$	0.322	0.334	0.338	0.472	0.526	0.556	1.033	1.138	0.979
$\beta_4^{(0)}$	−0.554	−0.497	−0.334	−0.623	−0.450	−0.071	−0.609	−0.463	−0.032
$\beta_5^{(0)}$	−0.195	−0.167	−0.128	−0.227	−0.173	−0.202	−0.112	−0.036	0.009
$\beta_6^{(0)}$	−0.101	−0.131	−0.114	−0.041	−0.049	0.037	0.183	0.198	0.205

TABLE V. T-type TMDC 1NN isotropic strain terms in units of eV.

	TiS_2	$TiSe_2$	$TiTe_2$	NbS_2	$NbSe_2$	$NbTe_2$	TaS_2	$TaSe_2$	$TaTe_2$
$t_0^{(1)}$	0.530	0.433	0.322	0.548	0.448	0.326	0.534	0.447	0.293
$t_1^{(1)}$	1.252	1.122	0.962	1.537	1.378	1.182	1.626	1.463	1.252
$t_2^{(1)}$	0.386	0.386	0.391	0.555	0.543	0.547	0.549	0.511	0.508
$t_3^{(1)}$	−0.698	−0.635	−0.565	−0.847	−0.772	−0.694	−0.925	−0.842	−0.766
$t_4^{(1)}$	−0.493	−0.441	−0.376	−0.597	−0.532	−0.437	−0.631	−0.559	−0.450
$t_5^{(1)}$	0.811	0.729	0.601	0.978	0.885	0.724	0.985	0.892	0.699
$t_6^{(1)}$	0.479	0.500	0.465	0.778	0.788	0.709	0.773	0.772	0.677
$t_7^{(1)}$	−0.574	−0.507	−0.423	−0.667	−0.586	−0.470	−0.756	−0.684	−0.575
$t_8^{(1)}$	0.220	0.201	0.194	0.145	0.135	0.128	0.190	0.186	0.179
$t_9^{(1)}$	−0.112	−0.102	−0.065	−0.127	−0.110	−0.052	−0.175	−0.169	−0.100
$t_{10}^{(1)}$	0.430	0.454	0.455	0.356	0.395	0.409	0.390	0.432	0.428
$t_{11}^{(1)}$	−0.363	−0.349	−0.292	−0.262	−0.262	−0.208	−0.285	−0.295	−0.228
$\alpha_0^{(1)}$	0.667	0.634	0.568	0.914	0.850	0.669	1.520	1.341	1.695
$\alpha_1^{(1)}$	−0.659	−0.454	−0.257	−0.380	−0.153	−0.032	−0.362	−0.221	−0.049
$\alpha_2^{(1)}$	−1.169	−1.002	−0.888	−1.274	−1.085	−0.945	−1.187	−1.033	−0.779
$\alpha_3^{(1)}$	0.750	0.624	0.516	0.538	0.396	0.302	0.927	0.785	0.709
$\alpha_4^{(1)}$	0.363	0.271	0.095	0.203	0.097	−0.121	−0.168	−0.189	−0.744
$\alpha_5^{(1)}$	−0.407	−0.289	−0.124	−0.175	−0.065	0.015	0.183	0.220	0.621
$\alpha_6^{(1)}$	−1.381	−1.214	−0.864	−1.750	−1.506	−1.052	−1.791	−1.513	−1.274
$\alpha_7^{(1)}$	0.281	0.187	0.025	−0.116	−0.210	−0.363	0.105	0.056	−0.076
$\alpha_8^{(1)}$	0.550	0.526	0.523	0.395	0.418	0.438	0.511	0.526	0.551
$\alpha_9^{(1)}$	−0.435	−0.420	−0.425	−0.413	−0.403	−0.388	−0.533	−0.515	−0.462
$\alpha_{10}^{(1)}$	−0.001	0.040	0.083	0.037	0.047	0.074	0.134	0.141	0.232
$\alpha_{11}^{(1)}$	−0.625	−0.617	−0.639	−0.539	−0.538	−0.551	−0.747	−0.746	−0.742

TABLE VI. *T*-type TMDC 1NN anisotropic strain terms in units of eV.

	TiS_2	$TiSe_2$	$TiTe_2$	NbS_2	$NbSe_2$	$NbTe_2$	TaS_2	$TaSe_2$	$TaTe_2$
$\beta_0^{(1)}$	0.129	0.193	0.208	0.423	0.482	0.445	1.069	1.102	0.805
$\beta_1^{(1)}$	−0.320	−0.115	0.019	0.071	0.282	0.294	1.094	1.197	0.952
$\beta_2^{(1)}$	−1.185	−1.115	−0.994	−1.398	−1.283	−1.125	−1.340	−1.191	−1.119
$\beta_3^{(1)}$	1.026	0.883	0.751	1.056	0.925	0.818	1.150	1.002	0.889
$\beta_4^{(1)}$	0.670	0.594	0.467	0.849	0.724	0.532	1.034	0.923	0.665
$\beta_5^{(1)}$	−0.736	−0.573	−0.326	−0.673	−0.441	−0.140	−0.336	−0.116	0.091
$\beta_6^{(1)}$	−0.400	−0.327	−0.242	−0.505	−0.335	−0.234	0.125	0.287	0.278
$\beta_7^{(1)}$	0.530	0.409	0.309	0.470	0.350	0.264	0.722	0.662	0.552
$\beta_8^{(1)}$	1.283	1.139	0.986	1.538	1.413	1.168	1.674	1.460	1.094
$\beta_9^{(1)}$	−0.263	−0.376	−0.430	−0.605	−0.762	−0.769	−1.513	−1.632	−1.380
$\beta_{10}^{(1)}$	0.792	0.672	0.515	0.867	0.742	0.551	0.807	0.670	0.492
$\beta_{11}^{(1)}$	0.530	0.444	0.272	0.626	0.512	0.275	0.424	0.283	0.083
$\beta_{12}^{(1)}$	0.119	0.125	0.132	0.270	0.237	0.256	0.219	0.180	0.143
$\beta_{13}^{(1)}$	0.752	0.707	0.591	1.079	1.035	0.809	1.028	0.926	0.648
$\beta_{14}^{(1)}$	−0.138	−0.209	−0.172	−0.349	−0.449	−0.296	−0.965	−1.137	−0.733
$\beta_{15}^{(1)}$	0.189	0.221	0.196	0.289	0.327	0.223	0.304	0.336	0.238
$\beta_{16}^{(1)}$	0.086	0.032	0.011	−0.105	−0.175	−0.112	−0.360	−0.430	−0.300
$\beta_{17}^{(1)}$	−0.371	−0.279	−0.221	−0.141	−0.028	−0.079	−0.236	−0.141	−0.212
$\beta_{18}^{(1)}$	0.028	−0.064	−0.161	−0.230	−0.327	−0.375	−0.336	−0.398	−0.407
$\beta_{19}^{(1)}$	0.080	0.074	0.033	0.107	0.081	0.031	0.192	0.169	0.076
$\beta_{20}^{(1)}$	−0.313	−0.287	−0.264	−0.155	−0.133	−0.108	−0.107	−0.092	−0.028

TABLE VII. *T*-type TMDC 2NN isotropic strain terms in units of eV.

	TiS_2	$TiSe_2$	$TiTe_2$	NbS_2	$NbSe_2$	$NbTe_2$	TaS_2	$TaSe_2$	$TaTe_2$
$t_0^{(2)}$	−0.067	−0.072	−0.040	−0.087	−0.089	−0.039	−0.077	−0.081	−0.026
$t_1^{(2)}$	0.701	0.782	0.883	0.732	0.831	0.982	0.762	0.842	0.989
$t_2^{(2)}$	−0.113	−0.137	−0.162	−0.159	−0.187	−0.219	−0.153	−0.176	−0.200
$t_3^{(2)}$	−0.050	−0.051	−0.051	−0.047	−0.048	−0.040	−0.076	−0.080	−0.071
$t_4^{(2)}$	0.015	0.019	0.030	0.039	0.040	0.046	0.062	0.065	0.072
$t_5^{(2)}$	−0.018	−0.034	−0.034	−0.036	−0.049	−0.037	−0.067	−0.085	−0.066
$t_6^{(2)}$	0.032	0.056	0.072	0.140	0.169	0.182	0.188	0.199	0.229
$t_7^{(2)}$	−0.125	−0.091	−0.074	−0.188	−0.121	−0.085	−0.205	−0.140	−0.079
$t_8^{(2)}$	−0.214	−0.201	−0.188	−0.467	−0.432	−0.398	−0.547	−0.486	−0.453
$t_9^{(2)}$	−0.021	−0.016	−0.004	−0.006	−0.005	0.011	−0.028	−0.028	−0.007
$t_{10}^{(2)}$	−0.103	−0.108	−0.113	−0.267	−0.263	−0.254	−0.313	−0.297	−0.304
$t_{11}^{(2)}$	0.210	0.166	0.141	0.339	0.265	0.225	0.365	0.282	0.222
$t_{12}^{(2)}$	0.114	0.088	0.070	0.158	0.117	0.082	0.162	0.121	0.074
$t_{13}^{(2)}$	−0.196	−0.182	−0.170	−0.387	−0.351	−0.316	−0.445	−0.395	−0.368
$t_{14}^{(2)}$	0.094	0.077	0.058	0.126	0.096	0.053	0.147	0.116	0.063
$\alpha_0^{(2)}$	0.059	0.036	−0.115	0.039	0.012	−0.168	−0.046	−0.076	−0.197
$\alpha_1^{(2)}$	−1.344	−1.493	−1.681	−1.329	−1.523	−1.822	−1.256	−1.403	−1.744
$\alpha_2^{(2)}$	0.408	0.464	0.548	0.493	0.557	0.672	0.396	0.438	0.534
$\alpha_3^{(2)}$	−0.104	−0.102	−0.118	−0.132	−0.130	−0.135	−0.191	−0.192	−0.138

TABLE VII. (*Continued*.)

	TiS_2	$TiSe_2$	$TiTe_2$	NbS_2	$NbSe_2$	$NbTe_2$	TaS_2	$TaSe_2$	$TaTe_2$
$\alpha_4^{(2)}$	−0.030	−0.023	−0.014	−0.077	−0.053	−0.005	−0.039	−0.030	0.028
$\alpha_5^{(2)}$	0.020	0.018	−0.031	−0.104	−0.088	−0.129	−0.114	−0.103	−0.176
$\alpha_6^{(2)}$	−0.581	−0.576	−0.536	−1.242	−1.177	−1.038	−1.608	−1.394	−1.389
$\alpha_7^{(2)}$	0.128	−0.006	−0.135	−0.258	−0.452	−0.529	−0.146	−0.296	−0.264
$\alpha_8^{(2)}$	0.944	0.835	0.722	1.608	1.418	1.188	1.885	1.613	1.387
$\alpha_9^{(2)}$	−0.202	−0.154	−0.119	−0.357	−0.248	−0.187	−0.422	−0.276	−0.291
$\alpha_{10}^{(2)}$	0.677	0.638	0.568	1.200	1.099	0.863	1.480	1.335	1.255
$\alpha_{11}^{(2)}$	−0.383	−0.284	−0.223	−0.292	−0.205	−0.192	−0.140	−0.125	−0.061
$\alpha_{12}^{(2)}$	−0.069	−0.024	0.031	0.127	0.163	0.202	0.377	0.341	0.604
$\alpha_{13}^{(2)}$	0.727	0.622	0.503	1.028	0.851	0.599	1.260	1.074	0.882
$\alpha_{14}^{(2)}$	−0.047	−0.000	0.089	0.227	0.253	0.351	0.389	0.372	0.649

TABLE VIII. T-type TMDC 2NN anisotropic strain terms in units of eV.

	TiS_2	$TiSe_2$	$TiTe_2$	NbS_2	$NbSe_2$	$NbTe_2$	TaS_2	$TaSe_2$	$TaTe_2$
$\beta_0^{(2)}$	−0.516	−0.570	−0.718	−0.544	−0.616	−0.839	−0.541	−0.595	−0.798
$\beta_1^{(2)}$	1.656	1.835	2.106	1.734	1.965	2.356	1.854	2.025	2.371
$\beta_2^{(2)}$	−0.439	−0.502	−0.573	−0.574	−0.655	−0.721	−0.526	−0.584	−0.592
$\beta_3^{(2)}$	−0.100	−0.121	−0.121	−0.152	−0.191	−0.151	−0.286	−0.320	−0.246
$\beta_4^{(2)}$	0.085	0.088	0.081	0.170	0.172	0.113	0.149	0.133	0.101
$\beta_5^{(2)}$	−0.024	−0.063	−0.035	−0.057	−0.119	−0.052	−0.175	−0.243	−0.150
$\beta_6^{(2)}$	0.475	0.524	0.610	0.489	0.561	0.705	0.521	0.577	0.731
$\beta_7^{(2)}$	0.034	0.023	0.027	0.036	0.020	0.027	0.137	0.130	0.129
$\beta_8^{(2)}$	−0.010	−0.021	−0.039	−0.008	−0.038	−0.074	−0.054	−0.088	−0.140
$\beta_9^{(2)}$	0.315	0.332	0.341	0.820	0.780	0.727	1.128	1.031	1.000
$\beta_{10}^{(2)}$	0.160	0.175	0.158	0.601	0.566	0.482	0.546	0.441	0.472
$\beta_{11}^{(2)}$	−0.922	−0.758	−0.622	−1.406	−1.140	−0.947	−1.544	−1.260	−1.187
$\beta_{12}^{(2)}$	0.019	0.002	−0.005	−0.066	−0.101	−0.120	−0.382	−0.410	−0.413
$\beta_{13}^{(2)}$	−0.233	−0.205	−0.152	−0.376	−0.340	−0.224	−0.446	−0.431	−0.381
$\beta_{14}^{(2)}$	0.464	0.357	0.269	0.516	0.389	0.272	0.474	0.363	0.182
$\beta_{15}^{(2)}$	0.127	0.100	0.037	0.121	0.103	−0.020	0.203	0.218	−0.028
$\beta_{16}^{(2)}$	−0.552	−0.470	−0.378	−0.868	−0.716	−0.540	−0.958	−0.812	−0.684
$\beta_{17}^{(2)}$	0.067	0.068	0.049	0.152	0.154	0.075	0.350	0.372	0.262
$\beta_{18}^{(2)}$	0.216	0.221	0.198	0.545	0.544	0.478	0.641	0.612	0.516
$\beta_{19}^{(2)}$	−0.130	−0.120	−0.145	−0.235	−0.220	−0.276	−0.312	−0.272	−0.339
$\beta_{20}^{(2)}$	0.167	0.149	0.117	0.392	0.365	0.281	0.394	0.339	0.248
$\beta_{21}^{(2)}$	−0.006	−0.013	−0.016	−0.061	−0.088	−0.086	−0.141	−0.144	−0.137
$\beta_{22}^{(2)}$	−0.076	−0.048	−0.030	−0.027	0.008	0.030	0.153	0.199	0.182
$\beta_{23}^{(2)}$	−0.161	−0.151	−0.111	−0.390	−0.368	−0.255	−0.451	−0.399	−0.220

TABLE IX. T-type TMDC 3NN isotropic strain terms in units of eV.

	TiS_2	$TiSe_2$	$TiTe_2$	NbS_2	$NbSe_2$	$NbTe_2$	TaS_2	$TaSe_2$	$TaTe_2$
$t_0^{(3)}$	−0.055	−0.054	−0.058	−0.077	−0.071	−0.075	−0.087	−0.078	−0.082
$t_1^{(3)}$	0.018	0.008	−0.014	−0.005	−0.015	−0.052	−0.016	−0.024	−0.067
$t_2^{(3)}$	0.037	0.051	0.063	0.093	0.107	0.120	0.095	0.102	0.109
$t_3^{(3)}$	−0.057	−0.052	−0.064	−0.048	−0.042	−0.061	−0.086	−0.079	−0.098
$t_4^{(3)}$	0.022	0.020	0.048	0.046	0.041	0.083	0.088	0.076	0.131
$t_5^{(3)}$	0.011	0.027	0.034	0.049	0.070	0.085	0.037	0.054	0.073
$t_6^{(3)}$	−0.060	−0.057	−0.083	−0.091	−0.089	−0.130	−0.125	−0.115	−0.163
$t_7^{(3)}$	0.014	0.008	0.000	−0.016	−0.023	−0.037	−0.013	−0.014	−0.025
$t_8^{(3)}$	−0.040	−0.041	−0.051	−0.044	−0.046	−0.055	−0.009	−0.011	−0.020
$t_9^{(3)}$	−0.086	−0.080	−0.068	−0.131	−0.119	−0.098	−0.153	−0.144	−0.123
$t_{10}^{(3)}$	−0.072	−0.073	−0.065	−0.089	−0.089	−0.061	−0.054	−0.050	−0.005
$t_{11}^{(3)}$	0.028	0.024	0.015	0.065	0.057	0.054	0.119	0.112	0.116
$\alpha_0^{(3)}$	0.314	0.266	0.233	0.242	0.194	0.169	0.334	0.276	0.119
$\alpha_1^{(3)}$	0.122	0.118	0.172	0.259	0.227	0.290	0.413	0.362	0.373
$\alpha_2^{(3)}$	−0.411	−0.429	−0.426	−0.520	−0.528	−0.492	−0.607	−0.614	−0.491
$\alpha_3^{(3)}$	0.024	0.009	−0.006	−0.097	−0.101	−0.117	−0.171	−0.139	−0.257
$\alpha_4^{(3)}$	−0.220	−0.201	−0.234	−0.301	−0.245	−0.216	−0.477	−0.447	−0.321
$\alpha_5^{(3)}$	−0.273	−0.317	−0.366	−0.423	−0.484	−0.571	−0.494	−0.525	−0.681
$\alpha_6^{(3)}$	0.323	0.306	0.345	0.377	0.352	0.313	0.528	0.511	0.414
$\alpha_7^{(3)}$	0.184	0.211	0.246	0.293	0.330	0.363	0.368	0.400	0.389
$\alpha_8^{(3)}$	0.054	0.051	0.068	0.088	0.094	0.112	0.073	0.115	0.086
$\alpha_9^{(3)}$	0.085	0.052	0.012	0.014	−0.034	−0.082	−0.006	−0.037	−0.095
$\alpha_{10}^{(3)}$	0.088	0.097	0.053	0.005	0.023	−0.018	−0.228	−0.232	−0.233
$\alpha_{11}^{(3)}$	−0.044	−0.022	−0.009	−0.065	−0.014	0.033	−0.220	−0.184	−0.118

TABLE X. T-type TMDC 3NN anisotropic strain terms in units of eV.

	TiS_2	$TiSe_2$	$TiTe_2$	NbS_2	$NbSe_2$	$NbTe_2$	TaS_2	$TaSe_2$	$TaTe_2$
$\beta_0^{(3)}$	0.524	0.515	0.559	0.625	0.593	0.674	0.709	0.668	0.708
$\beta_1^{(3)}$	−0.461	−0.424	−0.318	−0.565	−0.518	−0.333	−0.473	−0.427	−0.236
$\beta_2^{(3)}$	−0.096	−0.105	−0.095	−0.098	−0.102	−0.067	−0.111	−0.117	−0.074
$\beta_3^{(3)}$	−0.012	−0.015	−0.010	−0.085	−0.079	−0.061	−0.193	−0.184	−0.121
$\beta_4^{(3)}$	−0.135	−0.125	−0.136	−0.191	−0.175	−0.186	−0.092	−0.049	−0.096
$\beta_5^{(3)}$	−0.004	−0.054	−0.079	−0.051	−0.113	−0.159	0.006	−0.063	−0.138
$\beta_6^{(3)}$	0.240	0.231	0.238	0.327	0.314	0.333	0.489	0.438	0.457
$\beta_7^{(3)}$	0.110	0.133	0.178	0.234	0.256	0.305	0.306	0.318	0.376
$\beta_8^{(3)}$	0.158	0.138	0.160	0.223	0.209	0.284	0.249	0.228	0.271
$\beta_9^{(3)}$	0.073	0.076	0.005	0.178	0.144	−0.035	0.210	0.174	−0.053
$\beta_{10}^{(3)}$	−0.227	−0.226	−0.258	−0.330	−0.311	−0.339	−0.452	−0.426	−0.423
$\beta_{11}^{(3)}$	0.115	0.108	0.093	0.118	0.118	0.096	0.024	0.010	0.004
$\beta_{12}^{(3)}$	0.148	0.159	0.204	0.189	0.202	0.270	0.227	0.232	0.293
$\beta_{13}^{(3)}$	−0.120	−0.106	−0.131	−0.150	−0.132	−0.190	−0.290	−0.270	−0.261
$\beta_{14}^{(3)}$	−0.015	−0.018	0.010	0.003	0.004	0.078	0.138	0.159	0.174
$\beta_{15}^{(3)}$	−0.351	−0.350	−0.288	−0.560	−0.574	−0.419	−1.296	−1.281	−0.934
$\beta_{16}^{(3)}$	0.177	0.155	0.131	0.242	0.211	0.174	0.305	0.278	0.250

TABLE X. (*Continued*.)

	TiS_2	$TiSe_2$	$TiTe_2$	NbS_2	$NbSe_2$	$NbTe_2$	TaS_2	$TaSe_2$	$TaTe_2$
$\beta_{17}^{(3)}$	−0.036	−0.075	−0.105	−0.116	−0.189	−0.235	−0.336	−0.401	−0.365
$\beta_{18}^{(3)}$	−0.306	−0.308	−0.266	−0.508	−0.538	−0.461	−0.956	−0.979	−0.791
$\beta_{19}^{(3)}$	0.041	0.042	0.042	0.095	0.110	0.104	0.162	0.179	0.185
$\beta_{20}^{(3)}$	−0.030	−0.044	−0.026	−0.034	−0.042	0.011	−0.003	−0.013	0.066

[1] A. K. Geim and I. V. Grigorieva, Van der Waals heterostructures, Nature (London) **499**, 419 (2013).

[2] Q. H. Wang, K. Kalantar-Zadeh, A. Kis, J. N. Coleman, and M. S. Strano, Electronics and optoelectronics of two-dimensional transition metal dichalcogenides, Nat. Nanotechnol. **7**, 699 (2012).

[3] N. Zibouche, A. Kuc, J. Musfeldt, and T. Heine, Transition-metal dichalcogenides for spintronic applications, Ann. Phys. **526**, 395 (2014).

[4] X. Xu, W. Yao, D. Xiao, and T. F. Heinz, Spin and pseudospins in layered transition metal dichalcogenides, Nat. Phys. **10**, 343 (2014).

[5] M. T. Ong and E. J. Reed, Engineered piezoelectricity in graphene, ACS Nano **6**, 1387 (2012).

[6] A. A. Bukharaev, A. K. Zvezdin, A. P. Pyatakov, and Y. K. Fetisov, Straintronics: A new trend in micro- and nanoelectronics and materials science, Phys. Usp. **61**, 1175 (2018).

[7] S. Carr, D. Massatt, S. Fang, P. Cazeaux, M. Luskin, and E. Kaxiras, Twistronics: Manipulating the electronic properties of two-dimensional layered structures through their twist angle, Phys. Rev. B **95**, 075420 (2017).

[8] J. Lee, Z. Wang, K. He, J. Shan, and P. X.-L. Feng, High frequency MoS_2 nanomechanical resonators, ACS Nano **7**, 6086 (2013).

[9] R. E. Groenewald, M. Rösner, G. Schönhoff, S. Haas, and T. O. Wehling, Valley plasmonics in transition metal dichalcogenides, Phys. Rev. B **93**, 205145 (2016).

[10] T. Ritschel, J. Trinckauf, K. Koepernik, B. Büchner, M. v. Zimmermann, H. Berger, Y. Joe, P. Abbamonte, and J. Geck, Orbital textures and charge density waves in transition metal dichalcogenides, Nat. Phys. **11**, 328 (2015).

[11] J. T. Ye, Y. J. Zhang, R. Akashi, M. S. Bahramy, R. Arita, and Y. Iwasa, Superconducting dome in a gate-tuned band insulator, Science **338**, 1193 (2012).

[12] J. Zhang, J. M. Soon, K. P. Loh, J. Yin, J. Ding, M. B. Sullivian, and P. Wu, Magnetic molybdenum disulfide nanosheet films, Nano Lett. **7**, 2370 (2007).

[13] C. Gong, L. Li, Z. Li, H. Ji, A. Stern, Y. Xia, T. Cao, W. Bao, C. Wang, Y. Wang, Z. Q. Qiu, R. J. Cava, S. G. Louie, J. Xia, and X. Zhang, Discovery of intrinsic ferromagnetism in two-dimensional van der Waals crystals, Nature (London) **546**, 265 (2017).

[14] B. Huang, G. Clark, E. Navarro-Moratalla, D. R. Klein, R. Cheng, K. L. Seyler, D. Zhong, E. Schmidgall, M. A. McGuire, D. H. Cobden, W. Yao, D. Xiao, P. Jarillo-Herrero, and X. Xu, Layer-dependent ferromagnetism in a van der Waals crystal down to the monolayer limit, Nature (London) **546**, 270 (2017).

[15] X. Qian, J. Liu, L. Fu, and J. Li, Quantum spin Hall effect in two-dimensional transition metal dichalcogenides, Science **346**, 1344 (2014).

[16] S. Wu, V. Fatemi, Q. D. Gibson, K. Watanabe, T. Taniguchi, R. J. Cava, and P. Jarillo-Herrero, Observation of the quantum spin Hall effect up to 100 Kelvin in a monolayer crystal, Science **359**, 76 (2018).

[17] Y. Nakata, K. Sugawara, R. Shimizu, Y. Okada, P. Han, T. Hitosugi, K. Ueno, T. Sato, and T. Takahashi, Monolayer 1T-$NbSe_2$ as a Mott insulator, NPG Asia Mater. **8**, e321 (2016).

[18] L. Ma, C. Ye, Y. Yu, X. F. Lu, X. Niu, S. Kim, D. Feng, D. Tománek, Y.-W. Son, X. H. Chen, and Y. Zhang, A metallic mosaic phase and the origin of Mott-insulating state in 1T-TaS_2, Nat. Commun. **7**, 10956 (2016).

[19] K. T. Law and P. A. Lee, 1T-TaS_2 as a quantum spin liquid, Proc. Natl. Acad. Sci. U.S.A. **114**, 6996 (2017).

[20] H.-S. Kim, K. Haule, and D. Vanderbilt, Mott Metal-Insulator Transitions in Pressurized Layered Trichalcogenides, Phys. Rev. Lett. **123**, 236401 (2019).

[21] A. W. Tsen, R. Hovden, D. Wang, Y. D. Kim, J. Okamoto, K. A. Spoth, Y. Liu, W. Lu, Y. Sun, J. C. Hone, L. K. Kourkoutis, P. Kim, and A. N. Pasupathy, Structure and control of charge density waves in two-dimensional 1T-TaS_2, Proc. Natl. Acad. Sci. U.S.A. **112**, 15054 (2015).

[22] P. Fazekas and E. Tosatti, Electrical, structural and magnetic properties of pure and doped 1T-TaS_2, Philos. Mag. B **39**, 229 (1979).

[23] T. Ritschel, H. Berger, and J. Geck, Stacking-driven gap formation in layered 1T-TaS_2, Phys. Rev. B **98**, 195134 (2018).

[24] S.-H. Lee, J. S. Goh, and D. Cho, Origin of the Insulating Phase and First-Order Metal-Insulator Transition in 1T-TaS_2, Phys. Rev. Lett. **122**, 106404 (2019).

[25] Q. Stahl, M. Kusch, F. Heinsch, G. Garbarino, N. Kretzschmar, K. Hanff, K. Rossnagel, J. Geck, and T. Ritschel, Collapse of layer dimerization in the photo-induced hidden state of 1T-TaS_2, Nat. Commun. **11**, 1 (2020).

[26] B. Sipos, A. F. Kusmartseva, A. Akrap, H. Berger, L. Forró, and E. Tutiš, From Mott state to superconductivity in 1T-TaS_2, Nat. Mater. **7**, 960 (2008).

[27] R. Murray and A. Yoffe, The band structures of some transition metal dichalcogenides: Band structures of the titanium dichalcogenides, J. Phys. C: Solid State Phys. **5**, 3038 (1972).

[28] N. V. Smith, S. D. Kevan, and F. J. DiSalvo, Band structures of the layer compounds 1T-TaS_2 and 2H-$TaSe_2$ in the presence of commensurate charge-density waves, J. Phys. C: Solid State Phys. **18**, 3175 (1985).

[29] H. Rostami, R. Roldán, E. Cappelluti, R. Asgari, and F. Guinea, Theory of strain in single-layer transition metal dichalcogenides, Phys. Rev. B **92**, 195402 (2015).

[30] S. Fang, S. Carr, M. A. Cazalilla, and E. Kaxiras, Electronic structure theory of strained two-dimensional materials with hexagonal symmetry, Phys. Rev. B **98**, 075106 (2018).

[31] F. J. Di Salvo, D. Moncton, and J. Waszczak, Electronic properties and superlattice formation in the semimetal $TiSe_2$, Phys. Rev. B **14**, 4321 (1976).

[32] P. Chen, W. W. Pai, Y.-H. Chan, A. Takayama, C.-Z. Xu, A. Karn, S. Hasegawa, M.-Y. Chou, S.-K. Mo, A.-V. Fedorov *et al.*, Emergence of charge density waves and a pseudogap in single-layer $TiTe_2$, Nat. Commun. **8**, 516 (2017).

[33] C. Battaglia, H. Cercellier, F. Clerc, L. Despont, M. G. Garnier, C. Koitzsch, P. Aebi, H. Berger, L. Forró, and C. Ambrosch-Draxl, Fermi-surface-induced lattice distortion in $NbTe_2$, Phys. Rev. B **72**, 195114 (2005).

[34] J. Wilson, F. Di Salvo, and S. Mahajan, Charge-density waves and superlattices in the metallic layered transition metal dichalcogenides, Adv. Phys. **24**, 117 (1975); reprinted in **50**, 1171 (2001).

[35] J. Wilson, F. Di Salvo, and S. Mahajan, Charge-Density Waves in Metallic, Layered, Transition-Metal Dichalcogenides, Phys. Rev. Lett. **32**, 882 (1974).

[36] J. Feng, A. Tan, S. Wagner, J. Liu, Z. Mao, X. Ke, and P. Zhang, Charge modulation and structural transformation in $TaTe_2$ studied by scanning tunneling microscopy/spectroscopy, Appl. Phys. Lett. **109**, 021901 (2016).

[37] R. Kappera, D. Voiry, S. E. Yalcin, B. Branch, G. Gupta, A. D. Mohite, and M. Chhowalla, Phase-engineered low-resistance contacts for ultrathin MoS_2 transistors, Nat. Mater. **13**, 1128 (2014).

[38] J. Xia, J. Wang, D. Chao, Z. Chen, Z. Liu, J.-L. Kuo, J. Yan, and Z. X. Shen, Phase evolution of lithium intercalation dynamics in 2H-MoS_2, Nanoscale **9**, 7533 (2017).

[39] K.-A. N. Duerloo, Y. Li, and E. J. Reed, Structural phase transitions in two-dimensional Mo- and W-dichalcogenide monolayers, Nat. Commun. **5**, 4214 (2014).

[40] A. Nourbakhsh, A. Zubair, R. N. Sajjad, A. Tavakkoli KG, W. Chen, S. Fang, X. Ling, J. Kong, M. S. Dresselhaus, E. Kaxiras *et al.*, MoS_2 field-effect transistor with sub-10 nm channel length, Nano Lett. **16**, 7798 (2016).

[41] F. Bischoff, W. Auwärter, J. V. Barth, A. Schiffrin, M. Fuhrer, and B. Weber, Nanoscale phase engineering of niobium diselenide, Chem. Mater. **29**, 9907 (2017).

[42] S. J. McDonnell and R. M. Wallace, Atomically-thin layered films for device applications based upon 2D TMDC materials, Thin Solid Films **616**, 482 (2016).

[43] S. Manzeli, D. Ovchinnikov, D. Pasquier, O. V. Yazyev, and A. Kis, 2D transition metal dichalcogenides, Nat. Rev. Mater. **2**, 17033 (2017).

[44] D. Voiry, A. Mohite, and M. Chhowalla, Phase engineering of transition metal dichalcogenides, Chem. Soc. Rev. **44**, 2702 (2015).

[45] H. Cercellier, C. Monney, F. Clerc, C. Battaglia, L. Despont, M. G. Garnier, H. Beck, P. Aebi, L. Patthey, H. Berger, and L. Forró, Evidence for an Excitonic Insulator Phase in 1T-$TiSe_2$, Phys. Rev. Lett. **99**, 146403 (2007).

[46] E. Morosan, H. W. Zandbergen, B. Dennis, J. Bos, Y. Onose, T. Klimczuk, A. Ramirez, N. Ong, and R. J. Cava, Superconductivity in Cu_xTiSe_2, Nat. Phys. **2**, 544 (2006).

[47] L. Li, E. O'Farrell, K. Loh, G. Eda, B. Özyilmaz, and A. C. Neto, Controlling many-body states by the electric-field effect in a two-dimensional material, Nature (London) **529**, 185 (2016).

[48] M. Hellgren, J. Baima, R. Bianco, M. Calandra, F. Mauri, and L. Wirtz, Critical Role of the Exchange Interaction for the Electronic Structure and Charge-Density-Wave Formation in $TiSe_2$, Phys. Rev. Lett. **119**, 176401 (2017).

[49] C. M. Fang, R. A. De Groot, and C. Haas, Bulk and surface electronic structure of 1T−TiS_2 and 1T−$TiSe_2$, Phys. Rev. B **56**, 4455 (1997).

[50] P. Chen, Y.-H. Chan, X.-Y. Fang, S.-K. Mo, Z. Hussain, A.-V. Fedorov, M. Chou, and T.-C. Chiang, Hidden order and dimensional crossover of the charge density waves in $TiSe_2$, Sci. Rep. **6**, 37910 (2016).

[51] C. Xu, P. A. Brown, and K. L. Shuford, Strain-induced semimetal-to-semiconductor transition and indirect-to-direct band gap transition in monolayer 1T-TiS_2, RSC Adv. **5**, 83876 (2015).

[52] C. J. Carmalt, T. D. Manning, I. P. Parkin, E. S. Peters, and A. L. Hector, Formation of a new (1T) trigonal NbS_2 polytype via atmospheric pressure chemical vapour deposition, J. Mater. Chem. **14**, 290 (2004).

[53] M. Van Maaren and G. Schaeffer, Some new superconducting group V^a dichalcogenides, Phys. Lett. A **24**, 645 (1967).

[54] Y. Nakata, T. Yoshizawa, K. Sugawara, Y. Umemoto, T. Takahashi, and T. Sato, Selective fabrication of Mott-insulating and metallic monolayer $TaSe_2$, ACS Appl. Nano Mater. **1**, 1456 (2018).

[55] L. Li, W. Lu, X. Zhu, L. Ling, Z. Qu, and Y. Sun, Fe-doping-induced superconductivity in the charge-density-wave system 1T-TaS_2, Europhys. Lett. **97**, 67005 (2012).

[56] Y. Liu, R. Ang, W. Lu, W. Song, L. Li, and Y. Sun, Superconductivity induced by Se-doping in layered charge-density-wave system 1T-$TaS_{2-x}Se_x$, Appl. Phys. Lett. **102**, 192602 (2013).

[57] Y. Liu, D. F. Shao, L. J. Li, W. J. Lu, X. D. Zhu, P. Tong, R. C. Xiao, L. S. Ling, C. Y. Xi, L. Pi, H. F. Tian, H. X. Yang, J. Q. Li, W. H. Song, X. B. Zhu, and Y. P. Sun, Nature of charge density waves and superconductivity in 1T-$TaSe_{2-x}Te_x$, Phys. Rev. B **94**, 045131 (2016).

[58] G. Kresse and J. Furthmüller, Efficient iterative schemes for *ab initio* total-energy calculations using a plane-wave basis set, Phys. Rev. B **54**, 11169 (1996).

[59] G. Kresse and J. Furthmüller, Efficiency of *ab-initio* total energy calculations for metals and semiconductors using a plane-wave basis set, Comput. Mater. Sci. **6**, 15 (1996).

[60] J. P. Perdew, K. Burke, and M. Ernzerhof, Generalized Gradient Approximation Made Simple, Phys. Rev. Lett. **77**, 3865 (1996).

[61] S. Grimme, J. Antony, S. Ehrlich, and H. Krieg, A consistent and accurate *ab initio* parametrization of density functional dispersion correction (DFT-D) for the 94 elements H-Pu, J. Chem. Phys. **132**, 154104 (2010).

[62] A. A. Mostofi, J. R. Yates, Y.-S. Lee, I. Souza, D. Vanderbilt, and N. Marzari, WANNIER90: A tool for obtaining maximally-localised Wannier functions, Comput. Phys. Commun. **178**, 685 (2008).

[63] N. Marzari and D. Vanderbilt, Maximally localized generalized Wannier functions for composite energy bands, Phys. Rev. B **56**, 12847 (1997).

[64] I. Souza, N. Marzari, and D. Vanderbilt, Maximally localized Wannier functions for entangled energy bands, Phys. Rev. B **65**, 035109 (2001).

[65] H. Li, A. W. Contryman, X. Qian, S. M. Ardakani, Y. Gong, X. Wang, J. M. Weisse, C. H. Lee, J. Zhao, P. M. Ajayan *et al.*, Optoelectronic crystal of artificial atoms in strain-textured molybdenum disulphide, Nat. Commun. **6**, 7381 (2015).

[66] R. Banerjee, V.-H. Nguyen, T. Granzier-Nakajima, L. Pabbi, A. Lherbier, A. R. Binion, J.-C. Charlier, M. Terrones, and E. W. Hudson, Strain modulated superlattices in graphene, Nano Lett. **20**, 3113 (2020).

[67] T. B. Boykin and G. Klimeck, Practical application of zone-folding concepts in tight-binding calculations, Phys. Rev. B **71**, 115215 (2005).

[68] W. Ku, T. Berlijn, and C.-C. Lee, Unfolding First-Principles Band Structures, Phys. Rev. Lett. **104**, 216401 (2010).

[69] V. Popescu and A. Zunger, Extracting E versus $\boldsymbol{k}$ effective band structure from supercell calculations on alloys and impurities, Phys. Rev. B **85**, 085201 (2012).

[70] O. Rubel, A. Bokhanchuk, S. J. Ahmed, and E. Assmann, Unfolding the band structure of disordered solids: From bound states to high-mobility Kane fermions, Phys. Rev. B **90**, 115202 (2014).

[71] K. Rossnagel and N. V. Smith, Spin-orbit coupling in the band structure of reconstructed $1T$-TaS_2, Phys. Rev. B **73**, 073106 (2006).

[72] Y. Cao, V. Fatemi, A. Demir, S. Fang, S. L. Tomarken, J. Y. Luo, J. D. Sanchez-Yamagishi, K. Watanabe, T. Taniguchi, E. Kaxiras, R. C. Ashoori, and P. Jarillo-Herrero, Correlated insulator behaviour at half-filling in magic-angle graphene superlattices, Nature (London) **556**, 80 (2018).

[73] Y. Cao, V. Fatemi, S. Fang, K. Watanabe, T. Taniguchi, E. Kaxiras, and P. Jarillo-Herrero, Unconventional superconductivity in magic-angle graphene superlattices, Nature (London) **556**, 43 (2018).

[74] M. Yankowitz, S. Chen, H. Polshyn, Y. Zhang, K. Watanabe, T. Taniguchi, D. Graf, A. F. Young, and C. R. Dean, Tuning superconductivity in twisted bilayer graphene, Science **363**, 1059 (2019).

[75] N. N. T. Nam and M. Koshino, Lattice relaxation and energy band modulation in twisted bilayer graphene, Phys. Rev. B **96**, 075311 (2017).

[76] J. Jung, A. Raoux, Z. Qiao, and A. H. MacDonald, *Ab initio* theory of moiré superlattice bands in layered two-dimensional materials, Phys. Rev. B **89**, 205414 (2014).

[77] S. Fang and E. Kaxiras, Electronic structure theory of weakly interacting bilayers, Phys. Rev. B **93**, 235153 (2016).